Research Square

Preprints are preliminary reports that have not undergone peer review.
They should not be considered conclusive, used to inform clinical practice,
or referenced by the media as validated information.

A Fourier series solution for the free in-plane vibration of a rectangular plate with a straight through crack

Xutao Sun

xutao.sun@waikato.ac.nz

University of Waikato

Research Article

Keywords: Fourier series solutions, in-plane vibration, cracked rectangular plate, natural frequency, mode shape

Posted Date: August 5th, 2026

DOI: https://doi.org/10.21203/rs.3.rs-10493149/v1

License: This work is licensed under a Creative Commons Attribution 4.0 International License.
Read Full License

Additional Declarations: No competing interests reported.

A Fourier series solution for the free in-plane vibration of a rectangular plate with a straight through crack

Xutao Sun[a,*]
[a]The School of Engineering, University of Waikato, Hamilton, 3216, New Zealand
*Corresponding author.
E-mail address: xutao.sun@waikato.ac.nz
ORCID: 0000-0002-2874-7742

Abstract

In-plane vibration affects high-frequency energy transmission and the dynamic response of built-up plate structures. Although the transverse vibration of cracked plates has been widely studied, the corresponding in-plane vibration problem has received much less attention. Analytical-type benchmark solutions for the free in-plane vibration of cracked rectangular plates remain unavailable. The problem is more demanding than its out-of-plane counterpart due to the requirement of accommodating crack-induced discontinuities in two coupled displacement fields while simultaneously enforcing the governing equations, crack-face conditions, and boundary conditions. This study develops a Fourier series solution for isotropic plates containing a straight through side crack or internal crack under different combinations of classical boundary conditions. Domain decomposition is used to represent the displacement discontinuity across the crack, while the two coupled displacement components are represented by double Fourier cosine series supplemented by one-dimensional series that remove possible derivative discontinuities arising from periodic extension. The unknown Fourier coefficients are determined by matching the field equations and all interface and edge requirements, followed by a rank revealing reduction to a generalised eigenvalue problem. The formulation exhibits rapid and stable convergence. Its accuracy is confirmed through comparisons with published solutions for intact plates and finite element results for cracked plates. New frequency parameters and mode shapes are reported for cracks of different lengths and locations, which provide benchmark data for the in-plane vibration of cracked rectangular plates.

Keywords: Fourier series solutions; in-plane vibration; cracked rectangular plate; natural frequency; mode shape

1 Introduction

Rectangular plates are widely used structural components in aerospace, civil, mechanical, and marine engineering, including aircraft fuselage skin panels, ship hull and deck plating, machine parts, and building partitions. Their dynamic response comprises flexural motion normal to the middle plane and in plane motion associated with longitudinal and shear waves. While flexural vibration has received far greater attention, in-plane vibration is of substantial practical importance. Lyon (1986) showed that in-plane wave fields are a major carrier of structural noise, and Bercin (1996) demonstrated that they significantly influence high-frequency energy flow between coupled plate assemblies. Bardell *et al.* (1996) further established that in-plane modes can dominate the high-frequency dynamic response of plate structures, for example, ship hull panels subject to boundary-layer flow excitation and aircraft fuselage panels under turbulent loading (Gorman 2005). In-plane modes are also excited by tangential boundary loads and in-plane inertia forces in rotating components such as computer disk drives and circular saws (Leung *et al.* 1987, Chen 1996, Chen *et al.* 1996). Accurate characterisation of in-plane natural frequencies and mode shapes is therefore essential for vibro-acoustic design, resonance avoidance, and structural integrity assessment. These motivations become particularly acute when the plate contains damage such as a crack, which locally reduces stiffness and alters its dynamic characteristics.

The free in-plane vibration of intact isotropic rectangular plates has been studied through a variety of analytical and semi-analytical methods over several decades. Bardell *et al.* (1996) used the Rayleigh-Ritz method with K-orthogonal polynomials and Hermite cubics to establish important benchmarks for plates under various classical boundary conditions. Gorman subsequently developed a series of works using the superposition method, obtaining accurate analytical-type solutions for completely free, clamped, and simply supported rectangular plates (Gorman 2004, Gorman 2004), later extending this framework to orthotropic materials (Gorman 2009). Exact solutions via direct separation of variables were derived by Xing *et al.* (2009) for plates with at least one pair of opposite edges simply supported, a class of problems also addressed exactly by Gorman (2006). Regarding approximate and variational methods, Farag *et al.* (1999) utilised rod mode shapes and modal receptance functions to examine the coupling between longitudinal and shear waves, while Wang *et al.* (2002) solved the energy-based governing equations iteratively using the Kantorovich-Krylov method. Ritz methods employing trigonometric functions were further refined by Dozio (2010) to investigate plates with non-uniform elastic edge restraints. Furthermore, Du *et al.* (2007) introduced an improved Fourier series method to handle general elastically restrained and point-supported edges by incorporating supplementary

functions to remove potential derivative discontinuities at the edges under periodic extension. More recently, advanced frameworks such as the symplectic superposition method (Hu *et al.* 2023) has been implemented to provide analytical series-form solutions for increasingly complex boundary conditions.

After the intact-plate problem, cracked plates are the natural next step. The vibration of cracked plates has been studied far more extensively in the flexural (out-of-plane) context than in-plane, and the flexural literature provides useful methodological precedent. Early semi-analytical studies treated simply supported cracked plates using dual series equations reduced to homogeneous Fredholm integral equations of the second kind (Stahl *et al.* 1972), a subdomain formulation based on Fredholm integral equations of the first kind (Nezu 1982), and finite Fourier transforms of discontinuous displacement and slope fields with crack tip singularities incorporated into the solution (Solecki 1983). Finite element formulations later introduced specialised cracked plate elements whose stiffness matrices were derived from incorporating stress intensity factors (Qian *et al.* 1991) and additional crack induced flexibility (Krawczuk *et al.* 1994). Extended finite element methods (XFEM) represented displacement discontinuities by enriching conventional plate approximations, thereby avoiding the need for the mesh to conform closely to the crack geometry (Bachene *et al.* 2009, Natarajan *et al.* 2011). Within the Ritz framework, cracked plates were assembled from separate plate subdomains using artificial connecting springs (Yuan *et al.* 1992), while Liew *et al.* (1994) developed a domain decomposition method in which adjacent subdomains were coupled through continuity matrices. Other Ritz developments, for example, employed modified comparison functions constructed from Levy solutions (Khadem *et al.* 2000), regular polynomial bases supplemented by corner functions for side cracks and internal cracks (Huang *et al.* 2009, Huang *et al.* 2011), and admissible functions constructed by the moving least square method and corner functions for loaded internally cracked plates (Huang *et al.* 2018). Sun *et al.* (2024) similarly combined corner function enrichment with stress resultants obtained using XFEM to calculate the frequencies of loaded edge cracked plates. Domain decomposition was subsequently extended to cracked polygonal plates using Jacobi orthogonal polynomial Ritz expansions and spring-based coupling between subdomains (Song *et al.* 2022). Of particular relevance to the present study, Li *et al.* (2009) developed a Fourier series framework in which supplementary one dimensional series absorb derivative discontinuities at rectangular plate boundaries. Huang *et al.* (2016) then combined Fourier cosine series with domain decomposition, dividing side cracked and internally cracked rectangular plates into four and six subdomains, respectively, and enforcing continuity conditions between adjacent regions together with the boundary conditions on the external edges and crack faces. Chen *et al.* (2023) adopted a related four subdomain construction and applied double cosine finite integral transforms to edge cracked plates. These studies show that domain decomposition

combined with Fourier type representations offers a systematic analytical route for treating crack induced discontinuities while explicitly enforcing governing equations, external boundary conditions, and interface continuity.

Compared with the abundant literature on the out-of-plane dynamics of cracked plates, the free in-plane vibration of cracked rectangular plates has received very little attention. The in-plane problem is structurally distinct from and usually more demanding than its flexural counterpart. To the author's knowledge, the only accessible peer-reviewed study relevant to this topic appears to be the work of Zhong *et al.* (2023), who combined a substructure formulation, Chebyshev expansions, and the Rayleigh Ritz procedure to determine the modal and harmonic responses of complex shaped laminated plates containing cracks and irregular holes. However, analytical-type benchmark solutions remain unavailable for the free in-plane vibration of cracked rectangular plates. The present work fills this gap.

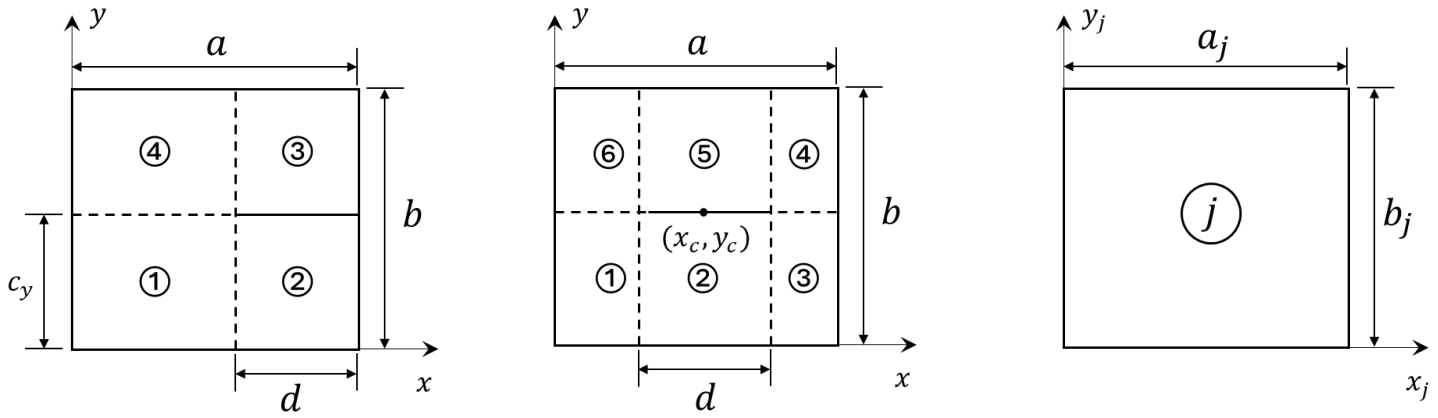
This study develops an analytical-type Fourier series formulation by combining domain decomposition with supplemented Fourier cosine series. A side cracked plate and an internally cracked plate are divided into four and six rectangular subdomains, respectively. The two in-plane displacement components in each subdomain are expressed by double Fourier cosine series supplemented by one-dimensional series that remove possible derivative discontinuities under periodic extension. The formulation considers the two coupled displacement components while systematically satisfies displacement and traction continuity between subdomains, the external boundary conditions, and the traction free conditions on crack faces. The complete coefficient system is reduced to a generalised eigenvalue problem, providing a unified treatment of side and internal cracks under different combinations of classical in plane boundary conditions. Convergence and accuracy are assessed using published results where available and finite element solutions where suitable reference data are unavailable. New natural frequency and mode shape results are then presented. Section 2 develops the formulation, Section 3 examines convergence and validation, Section 4 presents the parametric results, and Section 5 summarises the main conclusions.

2 Formulation

2.1 Fourier series solutions to governing equations

Consider an isotropic rectangular plate of length a, width b, thickness h, Young's modulus E, Poisson's ratio ν, and mass density ρ. The plate contains a straight through crack parallel to one of the plate edges. Depending on whether the crack is a side crack or an internal crack, the cracked plate is

decomposed into J rectangular subdomains, where $J = 4$ for a side-cracked plate and $J = 6$ for an internally cracked plate, following the domain-decomposition strategy used for cracked rectangular plates (as shown in Fig. 1).



(a) (b) (c)

Fig. 1. The dimensions and coordinates of cracked plates: (a) side-cracked plate; (b) internally cracked plate; (c) the j-th subdomain.

For the j-th subdomain, a local Cartesian coordinate system (x_j, y_j) is introduced, where $0 \le x_j \le a_j$ and $0 \le y_j \le b_j$ with a_j and b_j being the local length and width of the subdomain, respectively. The in-plane displacement components in the local x_j- and y_j-directions are denoted by $u^{(j)}(x_j, y_j)$ and $v^{(j)}(x_j, y_j)$, respectively. The harmonic displacement field is assumed in the form

$$\begin{aligned} u^{(j)}(x_j, y_j, t) &= u^{(j)}(x_j, y_j)e^{i\omega t} \\ v^{(j)}(x_j, y_j, t) &= v^{(j)}(x_j, y_j)e^{i\omega t} \end{aligned} \tag{1}$$

where ω is the circular natural frequency. Under plane-stress assumptions, the in-plane stresses are

$$\sigma_x^{(j)} = \frac{E}{1-\nu^2}\left(\frac{\partial u^{(j)}}{\partial x_j} + \nu\frac{\partial v^{(j)}}{\partial y_j}\right)$$
$$\sigma_y^{(j)} = \frac{E}{1-\nu^2}\left(\nu\frac{\partial u^{(j)}}{\partial x_j} + \frac{\partial v^{(j)}}{\partial y_j}\right) \tag{2}$$
$$\tau_{xy}^{(j)} = \frac{E}{2(1+\nu)}\left(\frac{\partial u^{(j)}}{\partial y_j} + \frac{\partial v^{(j)}}{\partial x_j}\right)$$

The governing differential equations for the free in-plane vibration of the j-th subdomain can be written as

$$\frac{\partial^2 u^{(j)}}{\partial x_j^2} + \mu\frac{\partial^2 u^{(j)}}{\partial y_j^2} + \eta\frac{\partial^2 v^{(j)}}{\partial x_j\,\partial y_j} + \Omega^2 u^{(j)} = 0$$
$$\frac{\partial^2 v^{(j)}}{\partial y_j^2} + \mu\frac{\partial^2 v^{(j)}}{\partial x_j^2} + \eta\frac{\partial^2 u^{(j)}}{\partial x_j\,\partial y_j} + \Omega^2 v^{(j)} = 0 \tag{3}$$

where $\mu = (1-\nu)/2$, $\eta = (1+\nu)/2$, and $\Omega^2 = \omega^2/c_L^2$ with $c_L = \sqrt{E/\rho(1-\nu^2)}$ being the longitudinal wave speed in the plate.

The displacement components in each subdomain can be expressed as a double Fourier cosine series supplemented by one-dimensional Fourier series multiplied by polynomial auxiliary functions. The purpose of the auxiliary terms is not to impose a specific boundary condition, but to remove possible discontinuities of the first derivatives when the displacement field is periodically extended outside the subdomain. For the j-th subdomain,

$$u^{(j)}(x_j, y_j) = \sum_{m=0}^{M}\sum_{n=0}^{N} A_{mn}^{(j)}\cos\lambda_m^{(j)}x_j\cos\beta_n^{(j)}y_j$$
$$+\chi_{1b}^{(j)}(y_j)\sum_{m=0}^{M} a_m^{(j)}\cos\lambda_m^{(j)}x_j + \chi_{2b}^{(j)}(y_j)\sum_{m=0}^{M} b_m^{(j)}\cos\lambda_m^{(j)}x_j \tag{4}$$
$$+\chi_{1a}^{(j)}(x_j)\sum_{n=0}^{N} c_n^{(j)}\cos\beta_n^{(j)}y_j + \chi_{2a}^{(j)}(x_j)\sum_{n=0}^{N} d_n^{(j)}\cos\beta_n^{(j)}y_j$$

and

$$
\begin{aligned}
v^{(j)}(x_j, y_j) &= \sum_{m=0}^{M}\sum_{n=0}^{N} B_{mn}^{(j)} \cos\lambda_m^{(j)} x_j \cos\beta_n^{(j)} y_j \\
&+\chi_{1b}^{(j)}(y_j)\sum_{m=0}^{M} e_m^{(j)} \cos\lambda_m^{(j)} x_j + \chi_{2b}^{(j)}(y_j)\sum_{m=0}^{M} f_m^{(j)} \cos\lambda_m^{(j)} x_j \\
&+\chi_{1a}^{(j)}(x_j)\sum_{n=0}^{N} g_n^{(j)} \cos\beta_n^{(j)} y_j + \chi_{2a}^{(j)}(x_j)\sum_{n=0}^{N} h_n^{(j)} \cos\beta_n^{(j)} y_j
\end{aligned} \tag{5}
$$

where $\lambda_m^{(j)} = m\pi/a_j$ and $\beta_n^{(j)} = n\pi/b_j$

The auxiliary functions are selected as

$$
\begin{aligned}
&\chi_{1a}^{(j)}(x_j) = a_j\xi_j(\xi_j - 1)^2, \qquad \chi_{2a}^{(j)}(x_j) = a_j\xi_j^2(\xi_j - 1), \qquad \xi_j = \frac{x_j}{a_j} \\
&\chi_{1b}^{(j)}(y_j) = b_j\eta_j(\eta_j - 1)^2, \qquad \chi_{2b}^{(j)}(y_j) = b_j\eta_j^2(\eta_j - 1), \qquad \eta_j = \frac{y_j}{b_j}
\end{aligned} \tag{6}
$$

These functions satisfy

$$
\begin{aligned}
&\chi_{1a}^{(j)}(0) = \chi_{1a}^{(j)}(a_j) = 0, \qquad \frac{d\chi_{1a}^{(j)}}{dx_j}(0) = 1, \qquad \frac{d\chi_{1a}^{(j)}}{dx_j}(a_j) = 0 \\
&\chi_{2a}^{(j)}(0) = \chi_{2a}^{(j)}(a_j) = 0, \qquad \frac{d\chi_{2a}^{(j)}}{dx_j}(0) = 0, \qquad \frac{d\chi_{2a}^{(j)}}{dx_j}(a_j) = 1
\end{aligned} \tag{7}
$$

with analogous relations for $\chi_{1b}^{(j)}$ and $\chi_{2b}^{(j)}$. Thus, the single Fourier series terms may be interpreted as terms introduced to absorb possible derivative jumps along the four edges of each rectangular subdomain.

Substituting Eqs. (4)-(5) into Eq. (3) yields

$$
\begin{aligned}
&-\sum_{m=0}^{M}\sum_{n=0}^{N}\left[\left(\lambda_m^{(j)}\right)^2+\mu\left(\beta_n^{(j)}\right)^2\right]A_{mn}^{(j)}\cos\lambda_m^{(j)}x_j\cos\beta_n^{(j)}y_j-\chi_{1b}^{(j)}(y_j)\sum_{m=0}^{M}\left(\lambda_m^{(j)}\right)^2 a_m^{(j)}\cos\lambda_m^{(j)}x_j-\chi_{2b}^{(j)}(y_j)\sum_{m=0}^{M}\left(\lambda_m^{(j)}\right)^2 b_m^{(j)}\cos\lambda_m^{(j)}x_j\\
&+\frac{d^2\chi_{1a}^{(j)}(x_j)}{dx_j^2}\sum_{n=0}^{N}c_n^{(j)}\cos\beta_n^{(j)}y_j+\frac{d^2\chi_{2a}^{(j)}(x_j)}{dx_j^2}\sum_{n=0}^{N}d_n^{(j)}\cos\beta_n^{(j)}y_j+\mu\left[\frac{d^2\chi_{1b}^{(j)}(y_j)}{dy_j^2}\sum_{m=0}^{M}a_m^{(j)}\cos\lambda_m^{(j)}x_j+\frac{d^2\chi_{2b}^{(j)}(y_j)}{dy_j^2}\sum_{m=0}^{M}b_m^{(j)}\cos\lambda_m^{(j)}x_j\right.\\
&\left.-\chi_{1a}^{(j)}(x_j)\sum_{n=0}^{N}\left(\beta_n^{(j)}\right)^2 c_n^{(j)}\cos\beta_n^{(j)}y_j-\chi_{2a}^{(j)}(x_j)\sum_{n=0}^{N}\left(\beta_n^{(j)}\right)^2 d_n^{(j)}\cos\beta_n^{(j)}y_j\right]+\eta\left[\sum_{m=0}^{M}\sum_{n=0}^{N}B_{mn}^{(j)}\lambda_m^{(j)}\beta_n^{(j)}\sin\lambda_m^{(j)}x_j\sin\beta_n^{(j)}y_j\right.\\
&\left.-\frac{d\chi_{1b}^{(j)}(y_j)}{dy_j}\sum_{m=0}^{M}e_m^{(j)}\lambda_m^{(j)}\sin\lambda_m^{(j)}x_j-\frac{d\chi_{2b}^{(j)}(y_j)}{dy_j}\sum_{m=0}^{M}f_m^{(j)}\lambda_m^{(j)}\sin\lambda_m^{(j)}x_j-\frac{d\chi_{1a}^{(j)}(x_j)}{dx_j}\sum_{n=0}^{N}g_n^{(j)}\beta_n^{(j)}\sin\beta_n^{(j)}y_j-\frac{d\chi_{2a}^{(j)}(x_j)}{dx_j}\sum_{n=0}^{N}h_n^{(j)}\beta_n^{(j)}\sin\beta_n^{(j)}y_j\right]\\
&+\Omega^2\left[\sum_{m=0}^{M}\sum_{n=0}^{N}A_{mn}^{(j)}\cos\lambda_m^{(j)}x_j\cos\beta_n^{(j)}y_j+\chi_{1b}^{(j)}(y_j)\sum_{m=0}^{M}a_m^{(j)}\cos\lambda_m^{(j)}x_j+\chi_{2b}^{(j)}(y_j)\sum_{m=0}^{M}b_m^{(j)}\cos\lambda_m^{(j)}x_j\right.\\
&\left.+\chi_{1a}^{(j)}(x_j)\sum_{n=0}^{N}c_n^{(j)}\cos\beta_n^{(j)}y_j+\chi_{2a}^{(j)}(x_j)\sum_{n=0}^{N}d_n^{(j)}\cos\beta_n^{(j)}y_j\right]=0
\end{aligned}
\tag{8}
$$

and

$$
\begin{aligned}
&-\sum_{m=0}^{M}\sum_{n=0}^{N}\left[\left(\beta_n^{(j)}\right)^2+\mu\left(\lambda_m^{(j)}\right)^2\right]B_{mn}^{(j)}\cos\lambda_m^{(j)}x_j\cos\beta_n^{(j)}y_j+\frac{d^2\chi_{1b}^{(j)}(y_j)}{dy_j^2}\sum_{m=0}^{M}e_m^{(j)}\cos\lambda_m^{(j)}x_j+\frac{d^2\chi_{2b}^{(j)}(y_j)}{dy_j^2}\sum_{m=0}^{M}f_m^{(j)}\cos\lambda_m^{(j)}x_j\\
&-\chi_{1a}^{(j)}(x_j)\sum_{n=0}^{N}\left(\beta_n^{(j)}\right)^2 g_n^{(j)}\cos\beta_n^{(j)}y_j-\chi_{2a}^{(j)}(x_j)\sum_{n=0}^{N}\left(\beta_n^{(j)}\right)^2 h_n^{(j)}\cos\beta_n^{(j)}y_j\\
&+\mu\left[-\chi_{1b}^{(j)}(y_j)\sum_{m=0}^{M}\left(\lambda_m^{(j)}\right)^2 e_m^{(j)}\cos\lambda_m^{(j)}x_j-\chi_{2b}^{(j)}(y_j)\sum_{m=0}^{M}\left(\lambda_m^{(j)}\right)^2 f_m^{(j)}\cos\lambda_m^{(j)}x_j+\frac{d^2\chi_{1a}^{(j)}(x_j)}{dx_j^2}\sum_{n=0}^{N}g_n^{(j)}\cos\beta_n^{(j)}y_j+\frac{d^2\chi_{2a}^{(j)}(x_j)}{dx_j^2}\sum_{n=0}^{N}h_n^{(j)}\cos\beta_n^{(j)}y_j\right]\\
&+\eta\left[\sum_{m=0}^{M}\sum_{n=0}^{N}A_{mn}^{(j)}\lambda_m^{(j)}\beta_n^{(j)}\sin\lambda_m^{(j)}x_j\sin\beta_n^{(j)}y_j-\frac{d\chi_{1b}^{(j)}(y_j)}{dy_j}\sum_{m=0}^{M}a_m^{(j)}\lambda_m^{(j)}\sin\lambda_m^{(j)}x_j-\frac{d\chi_{2b}^{(j)}(y_j)}{dy_j}\sum_{m=0}^{M}b_m^{(j)}\lambda_m^{(j)}\sin\lambda_m^{(j)}x_j\right.\\
&\left.-\frac{d\chi_{1a}^{(j)}(x_j)}{dx_j}\sum_{n=0}^{N}c_n^{(j)}\beta_n^{(j)}\sin\beta_n^{(j)}y_j-\frac{d\chi_{2a}^{(j)}(x_j)}{dx_j}\sum_{n=0}^{N}d_n^{(j)}\beta_n^{(j)}\sin\beta_n^{(j)}y_j\right]+\Omega^2\left[\sum_{m=0}^{M}\sum_{n=0}^{N}B_{mn}^{(j)}\cos\lambda_m^{(j)}x_j\cos\beta_n^{(j)}y_j\right.\\
&\left.+\chi_{1b}^{(j)}(y_j)\sum_{m=0}^{M}e_m^{(j)}\cos\lambda_m^{(j)}x_j+\chi_{2b}^{(j)}(y_j)\sum_{m=0}^{M}f_m^{(j)}\cos\lambda_m^{(j)}x_j+\chi_{1a}^{(j)}(x_j)\sum_{n=0}^{N}g_n^{(j)}\cos\beta_n^{(j)}y_j+\chi_{2a}^{(j)}(x_j)\sum_{n=0}^{N}h_n^{(j)}\cos\beta_n^{(j)}y_j\right]=0
\end{aligned}
\tag{9}
$$

In Eqs. (8)-(9), the sine terms and the polynomial auxiliary functions are not directly in the form of the double Fourier cosine basis. Therefore, these terms are further expanded into Fourier cosine series over the corresponding subdomain intervals. The auxiliary functions and their derivatives can be expanded as

$$
\begin{aligned}
&\chi_{ra}^{(j)}(x_j)=\sum_{m=0}^{M}\alpha_{rm}^{(j)}\cos\lambda_m^{(j)}x_j,\quad \frac{d\chi_{ra}^{(j)}(x_j)}{dx_j}=\sum_{m=0}^{M}\hat{\alpha}_{rm}^{(j)}\cos\lambda_m^{(j)}x_j,\quad \frac{d^2\chi_{ra}^{(j)}(x_j)}{dx_j^2}=\sum_{m=0}^{M}\tilde{\alpha}_{rm}^{(j)}\cos\lambda_m^{(j)}x_j\\
&\chi_{rb}^{(j)}(y_j)=\sum_{n=0}^{N}\gamma_{rn}^{(j)}\cos\beta_n^{(j)}y_j,\quad \frac{d\chi_{rb}^{(j)}(y_j)}{dy_j}=\sum_{n=0}^{N}\hat{\gamma}_{rn}^{(j)}\cos\beta_n^{(j)}y_j,\quad \frac{d^2\chi_{rb}^{(j)}(y_j)}{dy_j^2}=\sum_{n=0}^{N}\tilde{\gamma}_{rn}^{(j)}\cos\beta_n^{(j)}y_j
\end{aligned}
\tag{10}
$$

where $r=1,2$. The sine terms can be expanded as

$$\sin\lambda_p^{(j)} x_j = \sum_{m=0}^{M} S_{pm}^{x(j)} \cos\lambda_m^{(j)} x_j, \quad \sin\beta_q^{(j)} y_j = \sum_{n=0}^{N} S_{qn}^{y(j)} \cos\beta_n^{(j)} y_j \tag{11}$$

The Fourier coefficients in Eqs. (10)-(11) are determined in the usual way. For example,

$$\begin{aligned}
\alpha_{rm}^{(j)} &= \frac{\varepsilon_m}{a_j} \int_0^{a_j} \chi_{ra}^{(j)}(x_j) \cos\lambda_m^{(j)} x_j \, dx_j \\
\hat{\alpha}_{rm}^{(j)} &= \frac{\varepsilon_m}{a_j} \int_0^{a_j} \frac{d\chi_{ra}^{(j)}(x_j)}{dx_j} \cos\lambda_m^{(j)} x_j \, dx_j \\
\tilde{\alpha}_{rm}^{(j)} &= \frac{\varepsilon_m}{a_j} \int_0^{a_j} \frac{d^2\chi_{ra}^{(j)}(x_j)}{dx_j^2} \cos\lambda_m^{(j)} x_j \, dx_j \\
S_{pm}^{x(j)} &= \frac{\varepsilon_m}{a_j} \int_0^{a_j} \sin\lambda_p^{(j)} x_j \cos\lambda_m^{(j)} x_j \, dx_j
\end{aligned} \tag{12}$$

where $\varepsilon_0 = 1$ and $\varepsilon_m = 2$ when $m \geq 1$. The coefficients $\gamma_{rn}^{(j)}$, $\hat{\gamma}_{rn}^{(j)}$, $\tilde{\gamma}_{rn}^{(j)}$, and $S_{qn}^{y(j)}$ are defined analogously over $0 \leq y_j \leq b_j$. The closed-form expressions of the Fourier coefficients used in Eqs. (10)-(11) are given in Appendix A.

Substituting Eqs. (10)-(11) into Eqs. (8)-(9) and collecting the coefficients of the identical basis functions $\cos\lambda_m^{(j)} x_j \cos\beta_n^{(j)} y_j$ gives the following algebraic equations for $m = 0,1,\ldots,M$ and $n = 0,1,\ldots,N$:

$$\begin{aligned}
&\left[-\left(\lambda_m^{(j)}\right)^2 - \mu\left(\beta_n^{(j)}\right)^2 + \Omega^2\right] A_{mn}^{(j)} + \left[-\left(\lambda_m^{(j)}\right)^2 \gamma_{1n}^{(j)} + \mu\tilde{\gamma}_{1n}^{(j)} + \Omega^2\gamma_{1n}^{(j)}\right] a_m^{(j)} + \left[-\left(\lambda_m^{(j)}\right)^2 \gamma_{2n}^{(j)} + \mu\tilde{\gamma}_{2n}^{(j)} + \Omega^2\gamma_{2n}^{(j)}\right] b_m^{(j)} \\
&+ \left[\tilde{\alpha}_{1m}^{(j)} - \mu\left(\beta_n^{(j)}\right)^2 \alpha_{1m}^{(j)} + \Omega^2\alpha_{1m}^{(j)}\right] c_n^{(j)} + \left[\tilde{\alpha}_{2m}^{(j)} - \mu\left(\beta_n^{(j)}\right)^2 \alpha_{2m}^{(j)} + \Omega^2\alpha_{2m}^{(j)}\right] d_n^{(j)} + \eta \sum_{p=0}^{M}\sum_{q=0}^{N} B_{pq}^{(j)} \lambda_p^{(j)}\beta_q^{(j)} S_{pm}^{x(j)} S_{qn}^{y(j)} \\
&- \eta \sum_{p=0}^{M} e_p^{(j)} \lambda_p^{(j)} S_{pm}^{x(j)} \hat{\gamma}_{1n}^{(j)} - \eta \sum_{p=0}^{M} f_p^{(j)} \lambda_p^{(j)} S_{pm}^{x(j)} \hat{\gamma}_{2n}^{(j)} - \eta \sum_{q=0}^{N} g_q^{(j)} \beta_q^{(j)} \hat{\alpha}_{1m}^{(j)} S_{qn}^{y(j)} - \eta \sum_{q=0}^{N} h_q^{(j)} \beta_q^{(j)} \hat{\alpha}_{2m}^{(j)} S_{qn}^{y(j)} = 0
\end{aligned} \tag{13}$$

and

$$\left[-\left(\beta_n^{(j)}\right)^2-\mu\left(\lambda_m^{(j)}\right)^2+\Omega^2\right]B_{mn}^{(j)}+\left[\tilde{\gamma}_{1n}^{(j)}-\mu\left(\lambda_m^{(j)}\right)^2\gamma_{1n}^{(j)}+\Omega^2\gamma_{1n}^{(j)}\right]e_m^{(j)}+\left[\tilde{\gamma}_{2n}^{(j)}-\mu\left(\lambda_m^{(j)}\right)^2\gamma_{2n}^{(j)}+\Omega^2\gamma_{2n}^{(j)}\right]f_m^{(j)}$$
$$+\left[-\left(\beta_n^{(j)}\right)^2\alpha_{1m}^{(j)}+\mu\tilde{\alpha}_{1m}^{(j)}+\Omega^2\alpha_{1m}^{(j)}\right]g_n^{(j)}+\left[-\left(\beta_n^{(j)}\right)^2\alpha_{2m}^{(j)}+\mu\tilde{\alpha}_{2m}^{(j)}+\Omega^2\alpha_{2m}^{(j)}\right]h_n^{(j)}+\eta\sum_{p=0}^{M}\sum_{q=0}^{N}A_{pq}^{(j)}\lambda_p^{(j)}\beta_q^{(j)}S_{pm}^{x(j)}S_{qn}^{y(j)} \tag{14}$$
$$-\eta\sum_{p=0}^{M}a_p^{(j)}\lambda_p^{(j)}S_{pm}^{x(j)}\hat{\gamma}_{1n}^{(j)}-\eta\sum_{p=0}^{M}b_p^{(j)}\lambda_p^{(j)}S_{pm}^{x(j)}\hat{\gamma}_{2n}^{(j)}-\eta\sum_{q=0}^{N}c_q^{(j)}\beta_q^{(j)}\hat{\alpha}_{1m}^{(j)}S_{qn}^{y(j)}-\eta\sum_{q=0}^{N}d_q^{(j)}\beta_q^{(j)}\hat{\alpha}_{2m}^{(j)}S_{qn}^{y(j)}=0$$

To express Eqs. (13)-(14) in a matrix form, the equations are multiplied by -1, so that the frequency-dependent terms appear in the standard form ($\mathbf{K}-\Omega^2\mathbf{M}$). Let $R=(M+1)(N+1)$ and define the rearranged index $i=m(N+1)+n+1$. For the j-th subdomain, the double Fourier coefficient vectors are defined as

$$\mathbf{A}^{(j)}=\left[A_{00}^{(j)},A_{01}^{(j)},\dots,A_{0N}^{(j)},A_{10}^{(j)},A_{11}^{(j)},\dots,A_{MN}^{(j)}\right]^T$$
$$\mathbf{B}^{(j)}=\left[B_{00}^{(j)},B_{01}^{(j)},\dots,B_{0N}^{(j)},B_{10}^{(j)},B_{11}^{(j)},\dots,B_{MN}^{(j)}\right]^T \tag{15}$$

and

$$\mathbf{C}^{(j)}=\left[\mathbf{A}^{(j)T},\mathbf{B}^{(j)T}\right]^T \tag{16}$$

The coefficients associated with the supplementary terms are collected as

$$\mathbf{P}^{(j)}=\left[\mathbf{a}^{(j)T},\mathbf{b}^{(j)T},\mathbf{c}^{(j)T},\mathbf{d}^{(j)T},\mathbf{e}^{(j)T},\mathbf{f}^{(j)T},\mathbf{g}^{(j)T},\mathbf{h}^{(j)T}\right]^T \tag{17}$$

where

$$\mathbf{a}^{(j)}=[a_0^{(j)},a_1^{(j)},\dots,a_M^{(j)}]^T,\qquad \mathbf{b}^{(j)}=[b_0^{(j)},b_1^{(j)},\dots,b_M^{(j)}]^T$$
$$\mathbf{c}^{(j)}=[c_0^{(j)},c_1^{(j)},\dots,c_N^{(j)}]^T,\qquad \mathbf{d}^{(j)}=[d_0^{(j)},d_1^{(j)},\dots,d_N^{(j)}]^T \tag{18}$$

and similarly for $\mathbf{e}^{(j)}$, $\mathbf{f}^{(j)}$, $\mathbf{g}^{(j)}$, and $\mathbf{h}^{(j)}$.

Then Eqs. (13)-(14) can be written compactly as

$$\left(\widehat{\mathbf{K}}^{(j)}\mathbf{C}^{(j)}+\widetilde{\mathbf{K}}^{(j)}\mathbf{P}^{(j)}\right)-\Omega^2\left(\widehat{\mathbf{M}}^{(j)}\mathbf{C}^{(j)}+\widetilde{\mathbf{M}}^{(j)}\mathbf{P}^{(j)}\right)=\mathbf{0} \tag{19}$$

Here,

$$\widehat{\mathbf{K}}^{(j)} = \begin{bmatrix} \widehat{\mathbf{K}}_{AA}^{(j)} & \widehat{\mathbf{K}}_{AB}^{(j)} \\ \widehat{\mathbf{K}}_{BA}^{(j)} & \widehat{\mathbf{K}}_{BB}^{(j)} \end{bmatrix}, \qquad \widehat{\mathbf{M}}^{(j)} = \begin{bmatrix} \mathbf{I}_R & \mathbf{0} \\ \mathbf{0} & \mathbf{I}_R \end{bmatrix} \tag{20}$$

where $\mathbf{I}_R$ is an $R \times R$ identity matrix. For the row associated with (m, n) and the column associated with $(\bar{m}, \bar{n})$, the components of $\widehat{\mathbf{K}}^{(j)}$ are

$$\begin{aligned} \left(\widehat{\mathbf{K}}_{AA}^{(j)}\right)_{i\bar{i}} &= \left[\left(\lambda_m^{(j)}\right)^2 + \mu\left(\beta_n^{(j)}\right)^2\right]\delta_{m\bar{m}}\delta_{n\bar{n}} \\ \left(\widehat{\mathbf{K}}_{BB}^{(j)}\right)_{i\bar{i}} &= \left[\left(\beta_n^{(j)}\right)^2 + \mu\left(\lambda_m^{(j)}\right)^2\right]\delta_{m\bar{m}}\delta_{n\bar{n}} \\ \left(\widehat{\mathbf{K}}_{AB}^{(j)}\right)_{i\bar{i}} &= -\eta\lambda_{\bar{m}}^{(j)}\beta_{\bar{n}}^{(j)}S_{\bar{m}m}^{x(j)}S_{\bar{n}n}^{y(j)} \\ \left(\widehat{\mathbf{K}}_{BA}^{(j)}\right)_{i\bar{i}} &= -\eta\lambda_{\bar{m}}^{(j)}\beta_{\bar{n}}^{(j)}S_{\bar{m}m}^{x(j)}S_{\bar{n}n}^{y(j)} \end{aligned} \tag{21}$$

and $\delta_{m\bar{m}}$ and $\delta_{n\bar{n}}$ are Kronecker delta functions. The matrix $\widetilde{\mathbf{K}}^{(j)}$ contains the coefficients associated with the supplementary Fourier-series terms. It can be partitioned as

$$\widetilde{\mathbf{K}}^{(j)} = \begin{bmatrix} \widetilde{\mathbf{K}}_{ua}^{(j)} & \widetilde{\mathbf{K}}_{ub}^{(j)} & \widetilde{\mathbf{K}}_{uc}^{(j)} & \widetilde{\mathbf{K}}_{ud}^{(j)} & \widetilde{\mathbf{K}}_{ue}^{(j)} & \widetilde{\mathbf{K}}_{uf}^{(j)} & \widetilde{\mathbf{K}}_{ug}^{(j)} & \widetilde{\mathbf{K}}_{uh}^{(j)} \\ \widetilde{\mathbf{K}}_{va}^{(j)} & \widetilde{\mathbf{K}}_{vb}^{(j)} & \widetilde{\mathbf{K}}_{vc}^{(j)} & \widetilde{\mathbf{K}}_{vd}^{(j)} & \widetilde{\mathbf{K}}_{ve}^{(j)} & \widetilde{\mathbf{K}}_{vf}^{(j)} & \widetilde{\mathbf{K}}_{vg}^{(j)} & \widetilde{\mathbf{K}}_{vh}^{(j)} \end{bmatrix} \tag{22}$$

In Eq. (22), the representative components of the first block row, corresponding to the first governing equation, are

$$\begin{aligned} \left(\widetilde{\mathbf{K}}_{ua}^{(j)}\right)_{i\bar{m}} &= \left[\left(\lambda_m^{(j)}\right)^2\gamma_{1n}^{(j)} - \mu\tilde{\gamma}_{1n}^{(j)}\right]\delta_{m\bar{m}}, \quad \left(\widetilde{\mathbf{K}}_{ub}^{(j)}\right)_{i\bar{m}} = \left[\left(\lambda_m^{(j)}\right)^2\gamma_{2n}^{(j)} - \mu\tilde{\gamma}_{2n}^{(j)}\right]\delta_{m\bar{m}} \\ \left(\widetilde{\mathbf{K}}_{uc}^{(j)}\right)_{i\bar{n}} &= \left[\mu\left(\beta_n^{(j)}\right)^2\alpha_{1m}^{(j)} - \tilde{\alpha}_{1m}^{(j)}\right]\delta_{n\bar{n}}, \quad \left(\widetilde{\mathbf{K}}_{ud}^{(j)}\right)_{i\bar{n}} = \left[\mu\left(\beta_n^{(j)}\right)^2\alpha_{2m}^{(j)} - \tilde{\alpha}_{2m}^{(j)}\right]\delta_{n\bar{n}} \\ \left(\widetilde{\mathbf{K}}_{ue}^{(j)}\right)_{i\bar{m}} &= \eta\lambda_{\bar{m}}^{(j)}S_{\bar{m}m}^{x(j)}\hat{\gamma}_{1n}^{(j)}, \quad \left(\widetilde{\mathbf{K}}_{uf}^{(j)}\right)_{i\bar{m}} = \eta\lambda_{\bar{m}}^{(j)}S_{\bar{m}m}^{x(j)}\hat{\gamma}_{2n}^{(j)} \\ \left(\widetilde{\mathbf{K}}_{ug}^{(j)}\right)_{i\bar{n}} &= \eta\beta_{\bar{n}}^{(j)}\hat{\alpha}_{1m}^{(j)}S_{\bar{n}n}^{y(j)}, \quad \left(\widetilde{\mathbf{K}}_{uh}^{(j)}\right)_{i\bar{n}} = \eta\beta_{\bar{n}}^{(j)}\hat{\alpha}_{2m}^{(j)}S_{\bar{n}n}^{y(j)} \end{aligned} \tag{23}$$

The representative components of the second block row, corresponding to the second governing equation, are

$$\begin{aligned}
\left(\widetilde{\mathbf{K}}_{va}^{(j)}\right)_{i\bar{m}} &= \eta\lambda_{\bar{m}}^{(j)} S_{\bar{m}m}^{x(j)} \hat{\gamma}_{1n}^{(j)}, \quad \left(\widetilde{\mathbf{K}}_{vb}^{(j)}\right)_{i\bar{m}} = \eta\lambda_{\bar{m}}^{(j)} S_{\bar{m}m}^{x(j)} \hat{\gamma}_{2n}^{(j)} \\
\left(\widetilde{\mathbf{K}}_{vc}^{(j)}\right)_{i\bar{n}} &= \eta\beta_{\bar{n}}^{(j)} \hat{\alpha}_{1m}^{(j)} S_{\bar{n}n}^{y(j)}, \quad \left(\widetilde{\mathbf{K}}_{vd}^{(j)}\right)_{i\bar{n}} = \eta\beta_{\bar{n}}^{(j)} \hat{\alpha}_{2m}^{(j)} S_{\bar{n}n}^{y(j)} \\
\left(\widetilde{\mathbf{K}}_{ve}^{(j)}\right)_{i\bar{m}} &= \left[\mu\left(\lambda_m^{(j)}\right)^2 \gamma_{1n}^{(j)} - \tilde{\gamma}_{1n}^{(j)}\right]\delta_{m\bar{m}}, \quad \left(\widetilde{\mathbf{K}}_{vf}^{(j)}\right)_{i\bar{m}} = \left[\mu\left(\lambda_m^{(j)}\right)^2 \gamma_{2n}^{(j)} - \tilde{\gamma}_{2n}^{(j)}\right]\delta_{m\bar{m}} \\
\left(\widetilde{\mathbf{K}}_{vg}^{(j)}\right)_{i\bar{n}} &= \left[\left(\beta_n^{(j)}\right)^2 \alpha_{1m}^{(j)} - \mu\tilde{\alpha}_{1m}^{(j)}\right]\delta_{n\bar{n}}, \quad \left(\widetilde{\mathbf{K}}_{vh}^{(j)}\right)_{i\bar{n}} = \left[\left(\beta_n^{(j)}\right)^2 \alpha_{2m}^{(j)} - \mu\tilde{\alpha}_{2m}^{(j)}\right]\delta_{n\bar{n}}
\end{aligned} \tag{24}$$

The matrix $\widetilde{\mathbf{M}}^{(j)}$ contains the mass-like contributions from the supplementary terms and is partitioned in the same way as $\widetilde{\mathbf{K}}^{(j)}$. Its nonzero components are

$$\begin{aligned}
\left(\widetilde{\mathbf{M}}_{ua}^{(j)}\right)_{i\bar{m}} &= \gamma_{1n}^{(j)}\delta_{m\bar{m}}, \quad \left(\widetilde{\mathbf{M}}_{ub}^{(j)}\right)_{i\bar{m}} = \gamma_{2n}^{(j)}\delta_{m\bar{m}}, \quad \left(\widetilde{\mathbf{M}}_{uc}^{(j)}\right)_{i\bar{n}} = \alpha_{1m}^{(j)}\delta_{n\bar{n}}, \quad \left(\widetilde{\mathbf{M}}_{ud}^{(j)}\right)_{i\bar{n}} = \alpha_{2m}^{(j)}\delta_{n\bar{n}} \\
\left(\widetilde{\mathbf{M}}_{ve}^{(j)}\right)_{i\bar{m}} &= \gamma_{1n}^{(j)}\delta_{m\bar{m}}, \quad \left(\widetilde{\mathbf{M}}_{vf}^{(j)}\right)_{i\bar{m}} = \gamma_{2n}^{(j)}\delta_{m\bar{m}}, \quad \left(\widetilde{\mathbf{M}}_{vg}^{(j)}\right)_{i\bar{n}} = \alpha_{1m}^{(j)}\delta_{n\bar{n}}, \quad \left(\widetilde{\mathbf{M}}_{vh}^{(j)}\right)_{i\bar{n}} = \alpha_{2m}^{(j)}\delta_{n\bar{n}}
\end{aligned} \tag{25}$$

and all other components of $\widetilde{\mathbf{M}}^{(j)}$ are zero.

Combining Eq. (19) for all subdomains yields

$$\left(\widehat{\mathbf{K}}^*\mathbf{C}^* + \widetilde{\mathbf{K}}^*\mathbf{P}^*\right) - \Omega^2\left(\widehat{\mathbf{M}}^*\mathbf{C}^* + \widetilde{\mathbf{M}}^*\mathbf{P}^*\right) = \mathbf{0} \tag{26}$$

where

$$\mathbf{C}^* = \left[\mathbf{C}^{(1)T}, \mathbf{C}^{(2)T}, \ldots, \mathbf{C}^{(J)T}\right]^T, \quad \mathbf{P}^* = \left[\mathbf{P}^{(1)T}, \mathbf{P}^{(2)T}, \ldots, \mathbf{P}^{(J)T}\right]^T \tag{27}$$

and the global matrices are block diagonal:

$$\widehat{\mathbf{K}}^* = \begin{bmatrix} \widehat{\mathbf{K}}^{(1)} & \mathbf{0} & \cdots & \mathbf{0} \\ \mathbf{0} & \widehat{\mathbf{K}}^{(2)} & \cdots & \mathbf{0} \\ \vdots & \vdots & \ddots & \vdots \\ \mathbf{0} & \mathbf{0} & \cdots & \widehat{\mathbf{K}}^{(J)} \end{bmatrix}, \quad \widetilde{\mathbf{K}}^* = \begin{bmatrix} \widetilde{\mathbf{K}}^{(1)} & \mathbf{0} & \cdots & \mathbf{0} \\ \mathbf{0} & \widetilde{\mathbf{K}}^{(2)} & \cdots & \mathbf{0} \\ \vdots & \vdots & \ddots & \vdots \\ \mathbf{0} & \mathbf{0} & \cdots & \widetilde{\mathbf{K}}^{(J)} \end{bmatrix} \tag{28}$$

with analogous definitions for $\widehat{\mathbf{M}}^*$ and $\widetilde{\mathbf{M}}^*$. Equation (26) gives $2J(M+1)(N+1)$ algebraic equations obtained from the governing differential equations with $2J(M+1)(N+1) + 4J(M+1) + 4J(N+1)$ unknowns. Therefore, to solve for the unknowns, additional equations are required, which

are provided by the displacement and traction continuity conditions along the interconnection boundaries between adjacent subdomains and by the external boundary and crack-face conditions.

2.2 Continuity conditions

Along an interconnection boundary between two adjacent subdomains, both the in-plane displacement components and the corresponding traction components must be continuous. For a vertical interconnection boundary, the relevant traction components are σ_x and τ_{xy}, whereas for a horizontal interconnection boundary, they are σ_y and τ_{xy}. Considering subdomains 1 and 2 in Fig. 1, for example, the following continuity conditions should be satisfied:

$$\begin{aligned} u^{(1)}(a_1, y_1) &= u^{(2)}(0, y_2), \quad v^{(1)}(a_1, y_1) = v^{(2)}(0, y_2) \\ \sigma_x^{(1)}(a_1, y_1) &= \sigma_x^{(2)}(0, y_2), \quad \tau_{xy}^{(1)}(a_1, y_1) = \tau_{xy}^{(2)}(0, y_2) \end{aligned} \tag{29}$$

where $y_1 = y_2$. Substituting Eqs. (4)-(5) into the displacement continuity condition for u gives

$$\begin{aligned} &\sum_{m=0}^{M}\sum_{n=0}^{N}(-1)^m A_{mn}^{(1)}\cos\beta_n^{(1)} y_1 + \chi_{1b}^{(1)}(y_1)\sum_{m=0}^{M}(-1)^m a_m^{(1)} + \chi_{2b}^{(1)}(y_1)\sum_{m=0}^{M}(-1)^m b_m^{(1)} \\ &= \sum_{m=0}^{M}\sum_{n=0}^{N} A_{mn}^{(2)}\cos\beta_n^{(2)} y_2 + \chi_{1b}^{(2)}(y_2)\sum_{m=0}^{M} a_m^{(2)} + \chi_{2b}^{(2)}(y_2)\sum_{m=0}^{M} b_m^{(2)} \end{aligned} \tag{30}$$

Expanding the auxiliary functions in Eq. (30) into Fourier cosine series (Eq. (10)) and collecting the coefficients of $\cos\beta_n y$ yields

$$\gamma_{1n}^{(1)}\sum_{m=0}^{M}(-1)^m a_m^{(1)} + \gamma_{2n}^{(1)}\sum_{m=0}^{M}(-1)^m b_m^{(1)} - \gamma_{1n}^{(2)}\sum_{m=0}^{M} a_m^{(2)} - \gamma_{2n}^{(2)}\sum_{m=0}^{M} b_m^{(2)} = -\sum_{m=0}^{M}(-1)^m A_{mn}^{(1)} + \sum_{m=0}^{M} A_{mn}^{(2)}, \qquad n = 0,1,\dots,N \tag{31}$$

Similarly, the displacement continuity condition for v gives

$$\gamma_{1n}^{(1)}\sum_{m=0}^{M}(-1)^m e_m^{(1)} + \gamma_{2n}^{(1)}\sum_{m=0}^{M}(-1)^m f_m^{(1)} - \gamma_{1n}^{(2)}\sum_{m=0}^{M} e_m^{(2)} - \gamma_{2n}^{(2)}\sum_{m=0}^{M} f_m^{(2)} = -\sum_{m=0}^{M}(-1)^m B_{mn}^{(1)} + \sum_{m=0}^{M} B_{mn}^{(2)}, \qquad n = 0,1,\dots,N \tag{32}$$

Using Eq. (2), the traction continuity conditions can be written as

$$\left(\frac{\partial u^{(1)}}{\partial x_1}+\nu\frac{\partial v^{(1)}}{\partial y_1}\right)_{x_1=a_1}=\left(\frac{\partial u^{(2)}}{\partial x_2}+\nu\frac{\partial v^{(2)}}{\partial y_2}\right)_{x_2=0} \tag{33}$$

and

$$\left(\frac{\partial u^{(1)}}{\partial y_1}+\frac{\partial v^{(1)}}{\partial x_1}\right)_{x_1=a_1}=\left(\frac{\partial u^{(2)}}{\partial y_2}+\frac{\partial v^{(2)}}{\partial x_2}\right)_{x_2=0} \tag{34}$$

For the normal traction continuity condition, substituting Eqs. (4)-(5) into Eq. (33) gives

$$\begin{aligned} &d_n^{(1)}-c_n^{(2)}+\nu\left[\hat{\gamma}_{1n}^{(1)}\sum_{m=0}^{M}(-1)^m e_m^{(1)}+\hat{\gamma}_{2n}^{(1)}\sum_{m=0}^{M}(-1)^m f_m^{(1)}-\hat{\gamma}_{1n}^{(2)}\sum_{m=0}^{M}e_m^{(2)}-\hat{\gamma}_{2n}^{(2)}\sum_{m=0}^{M}f_m^{(2)}\right] \\ &=\nu\left[\sum_{m=0}^{M}\sum_{q=0}^{N}(-1)^m B_{mq}^{(1)}\beta_q^{(1)}S_{qn}^{y(1)}-\sum_{m=0}^{M}\sum_{q=0}^{N}B_{mq}^{(2)}\beta_q^{(2)}S_{qn}^{y(2)}\right], \quad n=0,1,\dots,N \end{aligned} \tag{35}$$

For the shear traction continuity condition, substituting Eqs. (4)-(5) into Eq. (34) gives

$$\begin{aligned} &h_n^{(1)}-g_n^{(2)}+\hat{\gamma}_{1n}^{(1)}\sum_{m=0}^{M}(-1)^m a_m^{(1)}+\hat{\gamma}_{2n}^{(1)}\sum_{m=0}^{M}(-1)^m b_m^{(1)}-\hat{\gamma}_{1n}^{(2)}\sum_{m=0}^{M}a_m^{(2)}-\hat{\gamma}_{2n}^{(2)}\sum_{m=0}^{M}b_m^{(2)} \\ &=\sum_{m=0}^{M}\sum_{q=0}^{N}(-1)^m A_{mq}^{(1)}\beta_q^{(1)}S_{qn}^{y(1)}-\sum_{m=0}^{M}\sum_{q=0}^{N}A_{mq}^{(2)}\beta_q^{(2)}S_{qn}^{y(2)}, \quad n=0,1,\dots,N \end{aligned} \tag{36}$$

Equations (31)-(32) and (35)-(36) provide $4(N+1)$ algebraic equations for a vertical interconnection boundary. In the same manner, for a horizontal interconnection boundary, for example between the top edge of subdomain 3 and the bottom edge of subdomain 4 in Fig. 1(b), the continuity conditions are

$$\begin{aligned} &u^{(3)}(x_3,b_3)=u^{(4)}(x_4,0), \qquad v^{(3)}(x_3,b_3)=v^{(4)}(x_4,0) \\ &\sigma_y^{(3)}(x_3,b_3)=\sigma_y^{(4)}(x_4,0), \qquad \tau_{xy}^{(3)}(x_3,b_3)=\tau_{xy}^{(4)}(x_4,0) \end{aligned} \tag{37}$$

where $x_3 = x_4$. These conditions yield $4(M+1)$ algebraic equations after the same Fourier coefficient comparison procedure. The detailed expressions of those equations are given in Appendix B.

2.3 Boundary conditions

The external boundary conditions are imposed on the outer edges of the subdomains. For a vertical external edge, the traction-free boundary conditions are

$$\sigma_x^{(j)} = 0, \qquad \tau_{xy}^{(j)} = 0 \tag{38}$$

whereas for a horizontal external edge,

$$\sigma_y^{(j)} = 0, \qquad \tau_{xy}^{(j)} = 0 \tag{39}$$

A clamped edge is described by

$$u^{(j)} = 0, \qquad v^{(j)} = 0 \tag{40}$$

For in-plane simply supported edges, two definitions may be introduced. If the normal displacement is restrained and the tangential traction is zero, then

$$u_n^{(j)} = 0, \qquad t_t^{(j)} = 0 \tag{41}$$

If the tangential displacement is restrained and the normal traction is zero, then

$$u_t^{(j)} = 0, \qquad t_n^{(j)} = 0 \tag{42}$$

The crack faces are traction-free. Therefore, for a horizontal crack face,

$$\sigma_y^{(j)} = 0, \qquad \tau_{xy}^{(j)} = 0 \tag{43}$$

whereas for a vertical crack face,

$$\sigma_x^{(j)} = 0, \qquad \tau_{xy}^{(j)} = 0 \tag{44}$$

The boundary and crack-face conditions are treated in the same way as the interconnection conditions. The displacement or traction expressions are obtained by substituting (4)-(5) into Eqs. (38)-(44), expanding the remaining non-cosine terms into Fourier cosine series, and collecting the coefficients of identical cosine terms. A vertical external boundary yields $2(N+1)$ equations, while a horizontal external boundary yields $2(M+1)$ equations.

Representative algebraic equations obtained from these boundary conditions are given in Appendix C. Collecting all continuity, boundary, and crack face equations gives the complete constraint system used in the rank revealing reduction described below.

2.4 Final eigenvalue equation

The algebraic equations obtained from the interconnection continuity conditions, external boundary conditions, and crack face conditions can be assembled as

$$\mathbf{G}_{\mathrm{C}}\mathbf{C}^{*}+\mathbf{G}_{\mathrm{P}}\mathbf{P}^{*}=\mathbf{0} \tag{45}$$

where $\mathbf{G}_{\mathrm{C}}$ and $\mathbf{G}_{\mathrm{P}}$ contain the coefficients associated with the double Fourier coefficients and supplementary Fourier coefficients, respectively. Define the complete coefficient vector and the complete constraint matrix as

$$\mathbf{q}^{*}=\begin{bmatrix}\mathbf{C}^{*}\\ \mathbf{P}^{*}\end{bmatrix},\qquad \mathbf{G}=[\mathbf{G}_{\mathrm{C}}\quad \mathbf{G}_{\mathrm{P}}] \tag{46}$$

Equation (45) can then be written compactly as

$$\mathbf{G}\mathbf{q}^{*}=\mathbf{0} \tag{47}$$

Let $n_{\mathrm{C}}=2J(M+1)(N+1)$ and $n_{\mathrm{P}}=4J(M+1)+4J(N+1)$ denote the numbers of double Fourier coefficients and supplementary Fourier coefficients, respectively. The complete constraint matrix $\mathbf{G}$ therefore contains n_{P} rows and $n_{\mathrm{C}}+n_{\mathrm{P}}$ columns. For directly imposed classical boundary conditions, the submatrix $\mathbf{G}_{\mathrm{P}}$ is not necessarily non-singular. Consequently, the supplementary coefficients cannot, in general, be eliminated independently of the double Fourier coefficients. Instead, the dependent coefficients are selected from the complete coefficient vector.

Provided that $\mathbf{G}$ has full row rank, a column permutation matrix $\mathbf{\Pi}=[\mathbf{\Pi}_{\mathrm{d}}\quad \mathbf{\Pi}_{\mathrm{f}}]$ can be selected such that

$$\mathbf{G}\mathbf{\Pi}=[\mathbf{U}\quad -\mathbf{D}] \tag{48}$$

where $\mathbf{U}=\mathbf{G}\mathbf{\Pi}_{\mathrm{d}}$ is an $n_{\mathrm{P}}\times n_{\mathrm{P}}$ non-singular matrix, while $-\mathbf{D}=\mathbf{G}\mathbf{\Pi}_{\mathrm{f}}$ contains the remaining n_{C} columns. The complete coefficient vector is correspondingly partitioned as

$$\mathbf{q}^{*}=\mathbf{\Pi}_{\mathrm{d}}\mathbf{q}_{\mathrm{d}}+\mathbf{\Pi}_{\mathrm{f}}\mathbf{z} \tag{49}$$

where $\mathbf{q}_\mathrm{d}$ contains the selected dependent coefficients and $\mathbf{z}$ is the vector of retained independent coefficients. The dependent vector may contain both double Fourier coefficients and supplementary Fourier coefficients.

Substitution of Eq. (49) into Eq. (47) gives

$$\mathbf{U}\mathbf{q}_\mathrm{d} = \mathbf{D}\mathbf{z} \tag{50}$$

Since $\mathbf{U}$ is non-singular,

$$\mathbf{q}_\mathrm{d} = \mathbf{U}^{-1}\mathbf{D}\mathbf{z} \tag{51}$$

The complete coefficient vector can therefore be expressed in terms of the independent coefficient vector as

$$\mathbf{q}^* = \mathbf{T}\mathbf{z} \tag{52}$$

where

$$\mathbf{T} = \mathbf{\Pi}_\mathrm{f} + \mathbf{\Pi}_\mathrm{d}\mathbf{U}^{-1}\mathbf{D} \tag{53}$$

Using Eq. (46), the assembled governing equation given by Eq. (26) can be written as

$$([\widehat{\mathbf{K}}^* \quad \widetilde{\mathbf{K}}^*] - \Omega^2[\widehat{\mathbf{M}}^* \quad \widetilde{\mathbf{M}}^*])\mathbf{q}^* = \mathbf{0} \tag{54}$$

Substituting Eq. (52) into Eq. (54) yields

$$(\mathbf{K}^* - \Omega^2\mathbf{M}^*)\mathbf{z} = \mathbf{0} \tag{55}$$

where

$$\mathbf{K}^* = [\widehat{\mathbf{K}}^* \quad \widetilde{\mathbf{K}}^*]\mathbf{T} \tag{56}$$

and

$$\mathbf{M}^* = [\widehat{\mathbf{M}}^* \quad \widetilde{\mathbf{M}}^*]\mathbf{T} \tag{57}$$

Equation (55) is a generalised eigenvalue problem of order n_C. A nontrivial solution exists when

$$\det(\mathbf{K}^* - \Omega^2\mathbf{M}^*) = 0 \tag{58}$$

When $\mathbf{G}_\mathrm{P}$ is non-singular, $\mathbf{\Pi}_\mathrm{d}$ may be chosen to select $\mathbf{P}^*$, while $\mathbf{\Pi}_\mathrm{f}$ selects $\mathbf{C}^*$. In this special case, $\mathbf{U} = \mathbf{G}_\mathrm{P}$, $\mathbf{D} = -\mathbf{G}_\mathrm{C}$, $\mathbf{z} = \mathbf{C}^*$, and Eq. (51) reduces to the direct elimination of the supplementary Fourier coefficients. The formulation above therefore includes the conventional supplementary coefficient elimination as a special case while remaining applicable when $\mathbf{G}_\mathrm{P}$ is singular.

In the numerical implementation, the independent and dependent columns are identified using a rank revealing QR factorisation of the complete constraint matrix. Solving Eq. (55) gives the eigenvalues Ω^2 and the corresponding independent coefficient vectors $\mathbf{z}$. The dependent coefficients are recovered from Eq. (51), after which the complete vector $\mathbf{q}^*$, and hence $\mathbf{C}^*$ and $\mathbf{P}^*$, are reconstructed from Eq. (49). The circular natural frequencies are obtained from $\omega = \Omega c_{\mathrm{L}}$. Finally, the corresponding in plane mode shapes are reconstructed by substituting the recovered Fourier coefficients into Eqs. (4)-(5).

3 Convergence studies

The convergence of the proposed formulation is examined by increasing the truncation numbers M and N. In the present calculations, a square truncation scheme with $M = N$ is adopted for simplicity. The convergence studies are performed first for intact plates, and then for side-cracked and internally cracked plates. The results are validated by comparing with published solutions or finite element results. A Poisson's ratio of 0.3 is considered for all the results shown hereafter. The boundary conditions for a rectangular plate are denoted by four letters, referring to the left edge, bottom edge, right edge, and top edge, respectively. Letters C and F represent clamped and free boundary conditions, respectively. As mentioned in Section 2.3, there are two definitions of in-plane simply supported edges, denoted here as S_1 and S_2. An S_1-type edge corresponds to zero displacement parallel to the edge and zero normal stress perpendicular to the edge, whereas the S_2-type edge corresponds to zero displacement normal to the edge and zero shear stress along the edge.

Table 1 gives the first eight frequency parameters of intact rectangular plates under selected boundary conditions. The plate is divided into four even subdomains similar to Fig. 1(a), and the continuity conditions are satisfied along the interconnection boundaries. Results with respect to $M = N =$4, 6, 8, 10, 12, and 14 are listed. Comparison with exact solutions (Xing and Liu 2009) and solutions obtained using the Ritz method (Dozio 2011) and the superposition method (Gorman 2005) is also presented. It can be observed that the frequency parameters converge rapidly and stabilise to the reported precision as $M = N$ increases, with changes beyond $M = N = 10$ confined to the third decimal place. Increasing $M = N$ beyond 10 produces only very small changes in the reported digits. In all cases, the current results are in excellent agreement with those in the literature. These comparisons confirm that the present formulation correctly reproduces the in-plane vibration behaviour of intact rectangular plates

Table 1. Convergence studies of frequency parameters for intact rectangular plates.

Boundary conditions	$M = N$	Mode No.							
		1	2	3	4	5	6	7	8
Frequency parameters $(\omega a/\pi)\sqrt{2\rho(1+\nu)/E}$; Aspect ratio $b/a = 1.2$									
S_1CS_1C	4	0.834	1.542	1.668	1.786	2.251	2.395	2.506	2.581
	6	0.834	1.541	1.667	1.785	2.250	2.393	2.502	2.576
	8	0.833	1.541	1.667	1.785	2.250	2.392	2.501	2.574
	10	0.833	1.541	1.667	1.785	2.249	2.392	2.500	2.574
	12	0.833	1.541	1.667	1.785	2.249	2.392	2.500	2.574
	14	0.833	1.541	1.667	1.785	2.249	2.392	2.500	2.574
	Xing and Liu (Xing and Liu 2009)	0.8333	1.5406	1.6667	1.7846	2.2493	2.3915	2.5000	2.5735
S_1CS_2F	4	0.737	0.904	1.398	1.526	1.961	2.041	2.293	2.414
	6	0.736	0.903	1.397	1.526	1.960	2.040	2.293	2.413
	8	0.736	0.903	1.397	1.525	1.960	2.040	2.292	2.412
	10	0.736	0.903	1.397	1.525	1.960	2.040	2.292	2.412
	12	0.736	0.903	1.397	1.525	1.960	2.040	2.292	2.412
	14	0.736	0.903	1.397	1.525	1.959	2.040	2.292	2.412
	Xing and Liu (Xing and Liu 2009)	0.7359	0.9029	1.3971	1.5252	1.9594	2.0398	2.2923	2.4121
Frequency parameters $\omega a\sqrt{\rho(1-\nu^2)/E}$; Aspect ratio $b/a = 1.0$									
$CCCC$	4	3.558	3.558	4.239	5.194	5.867	5.910	5.910	6.718
	6	3.556	3.556	4.236	5.189	5.862	5.899	5.899	6.711
	8	3.556	3.556	4.236	5.187	5.860	5.897	5.897	6.709
	10	3.555	3.555	4.235	5.186	5.859	5.896	5.896	6.709
	12	3.555	3.555	4.235	5.186	5.859	5.895	5.895	6.708
	14	3.555	3.555	4.235	5.186	5.859	5.895	5.895	6.708

	Dozio (Dozio 2010)	3.5552	3.5552	4.2350	5.1859	5.8587	5.8946	5.8946	6.7080
$FFFF$	4	2.322	2.476	2.476	2.632	2.993	3.454	3.725	3.725
	6	2.321	2.473	2.473	2.630	2.989	3.453	3.724	3.724
	8	2.321	2.472	2.472	2.631	2.988	3.452	3.723	3.725
	10	2.321	2.472	2.472	2.629	2.988	3.452	3.723	3.723
	12	2.321	2.472	2.472	2.629	2.988	3.452	3.723	3.723
	14	2.321	2.472	2.472	2.629	2.988	3.452	3.723	3.723
	Dozio (Dozio 2010)	2.3206	2.4716	2.4716	2.6284	2.9874	3.4522	3.7232	3.7232
Frequency parameters $(\omega a/2)\sqrt{\rho(1-\nu^2)/E}$; Aspect ratio $b/a = 1.0$									
$S_2S_2S_2S_2$	4	1.316	1.572	1.572	2.080	2.080	2.223	2.632	2.947
	6	1.315	1.571	1.571	2.079	2.079	2.222	2.630	2.941
	8	1.314	1.571	1.571	2.078	2.078	2.222	2.629	2.940
	10	1.314	1.571	1.571	2.078	2.078	2.222	2.629	2.939
	12	1.314	1.571	1.571	2.078	2.078	2.221	2.629	2.939
	14	1.314	1.571	1.571	2.078	2.078	2.221	2.629	2.939
	Gorman (Gorman 2005)	1.314	1.571	1.571	2.078	2.078	2.221	2.629	2.939

Table 2 presents the convergence results for side-cracked square plates with various boundary conditions. The ratios of crack length to edge length (d/a) are 0.2 and 0.5. Horizontal cracks at $c_y/b = 0.5$ in $S_2S_2S_2S_2$ and S_1CS_2F plates, and vertical cracks at $c_x/b = 0.5$ in S_2FS_1F plates are considered. Since there is no published numerical result for comparison, the commercial finite element software ANSYS Mechanical APDL is used to calculate dimensionless frequency parameters under the same conditions. The ANSYS results are obtained using two-dimensional elements (PLANE183). The KSCON command is employed to account for the crack tip singularity and refine the mesh near the crack tip. Convergence studies are performed on the ANSYS model to ensure the obtained results converge to the second decimal place. Table 2 shows that the current results converge fastly and are in good

agreement with ANSYS results. The leading two decimal places are essentially settled by $M = N = 10$, and the residual change between $M = N = 20$ and 22 remain within 0.001.

Table 2. Convergence studies of frequency parameters $(\omega a/2)\sqrt{\rho(1-\nu^2)/E}$ for side-cracked square plates under various boundary conditions.

Boundary conditions	d/a (or d/b)	$M = N$	Mode No.							
			1	2	3	4	5	6	7	8
$S_2S_2S_2S_2$	0.2	6	1.315	1.535	1.571	1.832	2.063	2.217	2.306	2.766
		8	1.314	1.535	1.571	1.835	2.063	2.217	2.307	2.766
		10	1.314	1.536	1.571	1.837	2.063	2.217	2.308	2.766
		12	1.314	1.536	1.571	1.838	2.063	2.217	2.308	2.766
		14	1.314	1.536	1.571	1.839	2.063	2.217	2.309	2.766
		16	1.314	1.536	1.571	1.840	2.064	2.217	2.309	2.766
		18	1.314	1.537	1.571	1.840	2.064	2.217	2.309	2.767
		20	1.314	1.537	1.571	1.841	2.064	2.217	2.309	2.767
		22	1.314	1.537	1.571	1.841	2.064	2.217	2.310	2.767
		Ansys	1.32	1.55	1.58	1.87	2.07	2.22	2.33	2.79
	0.5	6	1.315	1.413	1.571	1.676	1.867	2.157	2.242	2.285
		8	1.314	1.413	1.571	1.676	1.869	2.158	2.244	2.285
		10	1.314	1.413	1.571	1.676	1.870	2.158	2.245	2.285
		12	1.314	1.413	1.571	1.676	1.871	2.159	2.246	2.285
		14	1.314	1.413	1.571	1.676	1.872	2.159	2.246	2.285
		16	1.314	1.413	1.571	1.676	1.872	2.159	2.247	2.285
		18	1.314	1.413	1.571	1.676	1.873	2.159	2.247	2.285
		20	1.314	1.413	1.571	1.676	1.873	2.160	2.247	2.285
		22	1.314	1.413	1.571	1.676	1.873	2.160	2.248	2.285
		Ansys	1.32	1.42	1.58	1.68	1.89	2.17	2.27	2.31

S_1CS_2F	0.2	6	0.689	0.880	1.262	1.614	1.838	2.079	2.130	2.388
		8	0.690	0.880	1.263	1.614	1.840	2.079	2.129	2.388
		10	0.691	0.880	1.263	1.614	1.842	2.078	2.128	2.389
		12	0.692	0.880	1.263	1.614	1.843	2.078	2.128	2.389
		14	0.692	0.880	1.264	1.614	1.844	2.078	2.128	2.389
		16	0.693	0.880	1.264	1.614	1.844	2.078	2.128	2.390
		18	0.693	0.880	1.264	1.614	1.845	2.078	2.128	2.390
		20	0.693	0.880	1.264	1.614	1.845	2.078	2.128	2.390
		22	0.693	0.880	1.264	1.614	1.846	2.078	2.128	2.390
		Ansys	0.71	0.88	1.27	1.62	1.87	2.08	2.13	2.40
	0.5	6	0.405	0.873	1.166	1.576	1.636	1.984	2.055	2.225
		8	0.405	0.873	1.167	1.576	1.636	1.984	2.055	2.226
		10	0.406	0.873	1.167	1.577	1.637	1.985	2.055	2.227
		12	0.406	0.873	1.167	1.577	1.637	1.985	2.055	2.228
		14	0.406	0.873	1.168	1.577	1.637	1.985	2.055	2.228
		16	0.407	0.873	1.168	1.577	1.637	1.985	2.055	2.229
		18	0.407	0.873	1.168	1.577	1.637	1.985	2.055	2.229
		20	0.407	0.873	1.168	1.577	1.637	1.985	2.055	2.229
		22	0.407	0.873	1.168	1.577	1.637	1.985	2.055	2.229
		Ansys	0.42	0.88	1.18	1.58	1.65	2.00	2.06	2.25
S_2FS_1F	0.2	6	0.223	0.681	1.052	1.201	1.462	1.548	1.779	2.003
		8	0.223	0.681	1.053	1.201	1.462	1.548	1.783	2.007
		10	0.223	0.682	1.054	1.201	1.462	1.548	1.786	2.010
		12	0.223	0.682	1.055	1.201	1.462	1.548	1.788	2.012
		14	0.223	0.682	1.055	1.201	1.462	1.548	1.789	2.014

	16	0.224	0.683	1.056	1.201	1.462	1.548	1.790	2.015
	18	0.224	0.683	1.056	1.201	1.462	1.548	1.790	2.016
	20	0.224	0.683	1.056	1.201	1.462	1.548	1.791	2.017
	22	0.224	0.683	1.056	1.201	1.462	1.548	1.792	2.017
	Ansys	0.23	0.69	1.07	1.21	1.47	1.55	1.82	2.04
0.5	6	0.130	0.488	0.840	1.187	1.364	1.447	1.502	1.801
	8	0.130	0.489	0.842	1.187	1.365	1.447	1.502	1.801
	10	0.130	0.490	0.843	1.187	1.365	1.447	1.502	1.801
	12	0.130	0.490	0.844	1.187	1.366	1.447	1.503	1.801
	14	0.130	0.491	0.845	1.187	1.366	1.447	1.503	1.801
	16	0.130	0.491	0.845	1.187	1.366	1.447	1.503	1.801
	18	0.130	0.491	0.846	1.187	1.367	1.447	1.503	1.801
	20	0.130	0.491	0.846	1.187	1.367	1.447	1.503	1.801
	22	0.130	0.491	0.846	1.187	1.367	1.447	1.503	1.801
	Ansys	0.14	0.50	0.86	1.19	1.38	1.45	1.51	1.81

Table 3 presents the convergence results for square plates with central horizontal internal cracks under $S_2S_2S_2S_2$, S_1CS_2F, and S_2FS_1F boundary conditions, for which six domains are used. The crack length ratios $d/a = 0.2$ and $d/a = 0.5$ are again considered. The convergence behaviour mirrors that of the side-cracked case, remaining rapid and stable across all boundary conditions, and the converged parameters again agree well with the ANSYS results.

Table 3. Convergence studies of frequency parameters $(\omega a/2)\sqrt{\rho(1-\nu^2)/E}$ for square plates with central horizontal internal cracks under various boundary conditions.

Boundary conditions	d/a	$M=N$	Mode No.							
			1	2	3	4	5	6	7	8
$S_2S_2S_2S_2$	0.2	6	1.315	1.571	1.571	2.076	2.078	2.158	2.396	2.732
		8	1.315	1.571	1.571	2.076	2.077	2.162	2.401	2.740
		10	1.314	1.571	1.571	2.076	2.077	2.165	2.403	2.746
		12	1.314	1.571	1.571	2.076	2.077	2.166	2.405	2.749
		14	1.314	1.571	1.571	2.076	2.077	2.167	2.406	2.752
		16	1.314	1.571	1.571	2.076	2.077	2.168	2.407	2.754
		18	1.314	1.571	1.571	2.076	2.077	2.169	2.408	2.755
		20	1.314	1.571	1.571	2.076	2.077	2.169	2.409	2.757
		22	1.314	1.571	1.571	2.076	2.077	2.170	2.410	2.758
		Ansys	1.32	1.58	1.58	2.08	2.08	2.19	2.47	2.80
	0.5	6	1.315	1.566	1.571	1.839	1.887	2.017	2.036	2.541
		8	1.315	1.565	1.571	1.840	1.892	2.019	2.036	2.541
		10	1.314	1.565	1.571	1.841	1.895	2.020	2.036	2.542
		12	1.314	1.565	1.571	1.841	1.898	2.021	2.036	2.542
		14	1.314	1.565	1.571	1.842	1.899	2.021	2.036	2.543
		16	1.314	1.565	1.571	1.842	1.900	2.022	2.036	2.543
		18	1.314	1.565	1.571	1.842	1.901	2.022	2.036	2.543
		20	1.314	1.565	1.571	1.842	1.902	2.022	2.036	2.543
		22	1.314	1.565	1.571	1.843	1.903	2.023	2.036	2.543
		Ansys	1.32	1.57	1.58	1.88	1.94	2.04	2.05	2.55
S_1CS_2F	0.2	6	0.771	0.876	1.293	1.594	2.029	2.086	2.153	2.468

		8	0.771	0.876	1.294	1.596	2.030	2.087	2.153	2.470
		10	0.771	0.876	1.294	1.596	2.031	2.088	2.153	2.472
		12	0.772	0.876	1.295	1.597	2.032	2.089	2.153	2.473
		14	0.772	0.876	1.295	1.597	2.032	2.089	2.154	2.473
		16	0.772	0.876	1.295	1.597	2.032	2.089	2.154	2.474
		18	0.772	0.876	1.296	1.598	2.033	2.089	2.154	2.474
		20	0.772	0.876	1.296	1.598	2.033	2.090	2.154	2.475
		22	0.772	0.876	1.296	1.598	2.033	2.090	2.154	2.475
		Ansys	0.78	0.88	1.30	1.60	2.05	2.10	2.16	2.50
	0.5	6	0.639	0.856	1.178	1.478	1.771	2.023	2.093	2.246
		8	0.639	0.856	1.179	1.480	1.772	2.024	2.094	2.249
		10	0.640	0.856	1.180	1.482	1.772	2.024	2.094	2.250
		12	0.640	0.857	1.181	1.483	1.772	2.025	2.094	2.251
		14	0.640	0.857	1.181	1.484	1.772	2.025	2.094	2.252
		16	0.640	0.857	1.181	1.484	1.773	2.025	2.095	2.253
		18	0.641	0.857	1.182	1.485	1.773	2.025	2.095	2.253
		20	0.641	0.857	1.182	1.485	1.773	2.025	2.095	2.254
		22	0.641	0.857	1.182	1.485	1.773	2.025	2.095	2.254
		Ansys	0.65	0.86	1.19	1.50	1.79	2.04	2.10	2.27
S_2FS_1F	0.2	6	0.255	0.740	1.138	1.205	1.356	1.548	2.043	2.080
		8	0.255	0.740	1.139	1.205	1.358	1.548	2.045	2.080
		10	0.255	0.740	1.141	1.206	1.360	1.548	2.046	2.080
		12	0.255	0.740	1.141	1.206	1.361	1.548	2.046	2.080
		14	0.255	0.740	1.142	1.206	1.361	1.548	2.047	2.080
		16	0.255	0.740	1.142	1.206	1.362	1.548	2.047	2.080
		18	0.255	0.740	1.142	1.206	1.362	1.548	2.048	2.080

	20	0.255	0.740	1.143	1.206	1.363	1.548	2.048	2.080
	22	0.255	0.740	1.143	1.207	1.363	1.548	2.048	2.081
	Ansys	0.26	0.74	1.16	1.21	1.39	1.55	2.07	2.08
0.5	6	0.243	0.734	0.911	0.999	1.173	1.481	1.957	2.033
	8	0.243	0.734	0.913	1.002	1.173	1.481	1.958	2.033
	10	0.243	0.734	0.914	1.004	1.174	1.481	1.959	2.033
	12	0.244	0.734	0.914	1.005	1.174	1.482	1.960	2.033
	14	0.244	0.734	0.915	1.006	1.175	1.482	1.960	2.033
	16	0.244	0.734	0.915	1.006	1.175	1.482	1.960	2.033
	18	0.244	0.734	0.915	1.007	1.175	1.482	1.961	2.033
	20	0.244	0.734	0.916	1.007	1.175	1.482	1.961	2.033
	22	0.244	0.734	0.916	1.008	1.175	1.482	1.961	2.033
	Ansys	0.25	0.74	0.95	1.03	1.18	1.50	1.98	2.04

Because the supplemented cosine series can be differentiated term by term and, in the limit of large M and N, satisfies the governing equations together with all continuity, external-boundary, and crack-face conditions, the present solution can in principle be evaluated to any prescribed accuracy. The approach to the converged value is not one-sided: the intact-plate parameters approach from above, whereas individual cracked-plate modes may approach from above or below, so the present results do not constitute lower or upper bounds. In practice, convergence is rapid in every case considered. Based on Table 1 to Table 3, $M = N = 20$ is adopted in the subsequent calculations. This truncation reproduces the converged frequency parameters to the second decimal place reported in Section 4 while substantially reducing the size of the global constraint and eigenvalue systems relative to higher truncations, a consideration that is particularly important for the six-subdomain internally cracked model.

4 Results and discussion

The convergence studies have shown that the proposed Fourier series formulation gives stable frequency estimates for intact, side-cracked, and internally cracked rectangular plates. On this basis, the present section applies the formulation to examine the effects of crack length, crack location, and boundary conditions on the first eight in-plane frequency parameters. Selected mode shapes are also presented to illustrate the changes in the displacement field. The modes are numbered according to ascending frequency. Since crack growth may separate repeated frequencies or change the ordering of closely spaced modes, the frequency results should be interpreted together with the corresponding mode shapes. The results are presented first for side-cracked rectangular plates and then for internally cracked square plates.

4.1 Side-cracked rectangular plates

Table 4 to Table 6 present the first eight frequency parameters of side-cracked rectangular plates under three representative boundary conditions. Horizontal side cracks are considered for $S_2S_2S_2S_2$ plates, while vertical side cracks are considered for S_1CS_2F and S_2FS_1F plates. The crack length ratio is varied from the intact condition 0.5. Table 7 presents the first four mode shapes for selected square plates to assist the interpretation of the frequency variations.

A primary observation across all tables is that the ordered frequency parameters are non-increasing with crack length, although their sensitivity differs considerably among modes. For example, in Table 4 for an $S_2S_2S_2S_2$ square plate with a crack at $c_y/b = 0.5$, the first and third frequency parameters remain unchanged to the reported precision as the crack length increases to $d/a = 0.5$. In contrast, the fourth, seventh, and eighth parameters decrease by approximately 19%, 14%, and 22%, respectively. This differential sensitivity suggests that a mode is most affected when the crack lies in a region of high modal strain energy for that specific vibration shape.

The influence of crack location can be observed by comparing the cases $c_y/b = 0.5$ and $c_y/b = 0.75$ in Table 4. As the crack moves away from the centerline, its impact on specific modes changes. For the first mode, the frequency reduction is more significant when the crack is at $c_y/b = 0.75$ (dropping from 1.31 to 1.09) than when it is at the center, where the fundamental parameter is nearly unchanged. This indicates that, for S_2-type boundary conditions, the edges near the corners may represent regions of higher influence for the first mode's stiffness.

Table 4. Frequency parameters $(\omega a/2)\sqrt{\rho(1-\nu^2)/E}$ for $S_2S_2S_2S_2$ rectangular plates with horizontal side cracks of various lengths at different locations.

b/a	c_y/b	d/a	Mode No.							
			1	2	3	4	5	6	7	8
1	0.5	0	1.31	1.57	1.57	2.08	2.08	2.22	2.63	2.94
		0.1	1.31	1.56	1.57	2.03	2.08	2.22	2.51	2.91
		0.2	1.31	1.54	1.57	1.84	2.06	2.22	2.31	2.77
		0.3	1.31	1.48	1.57	1.72	2.02	2.20	2.28	2.71
		0.4	1.31	1.44	1.57	1.69	1.95	2.19	2.28	2.53
		0.5	1.31	1.41	1.57	1.68	1.87	2.16	2.25	2.29
	0.75	0.1	1.30	1.54	1.57	2.06	2.08	2.19	2.63	2.89
		0.2	1.24	1.48	1.57	2.00	2.07	2.15	2.63	2.79
		0.3	1.17	1.44	1.57	1.96	2.07	2.13	2.63	2.75
		0.4	1.12	1.42	1.57	1.90	2.06	2.12	2.63	2.71
		0.5	1.09	1.40	1.57	1.80	2.03	2.10	2.63	2.67
1.2	0.75	0	1.21	1.31	1.57	1.81	2.01	2.04	2.42	2.50
		0.1	1.19	1.29	1.57	1.81	1.99	2.03	2.42	2.48
		0.2	1.14	1.27	1.56	1.80	1.92	2.02	2.42	2.43
		0.3	1.07	1.25	1.55	1.79	1.87	2.01	2.40	2.42
		0.4	1.01	1.24	1.55	1.76	1.85	2.00	2.38	2.41
		0.5	0.97	1.23	1.55	1.70	1.84	1.97	2.37	2.41

The influence of boundary conditions is further highlighted in Table 5 (S_1CS_2F) and Table 6 (S_2FS_1F). For the S_1CS_2F plate, the fundamental frequency is far more sensitive to the crack length than in the $S_2S_2S_2S_2$ case, showing a drop of about 39% at $c_x/a = 0.5$ as d/b reaches 0.5. This suggests that the presence of a crack near a clamped edge (C) or a free edge (F) can cause a more significant redistribution of the internal stress field compared to plates

with fully simply supports. The S_2FS_1F results in Table 6 show the strongest crack sensitivity among the side cracked cases considered. The intact square plate has a low first frequency parameter of 0.26, reflecting the relatively flexible support condition. When a vertical crack at $c_x/a = 0.5$ grows to $d/b = 0.5$, the first frequency parameter decreases to 0.13, while for $c_x/a = 0.75$, the same crack length gives 0.17. The reduction remains significant for several higher modes. For example, in the square plate with $c_x/a = 0.75$, the second frequency parameter reduces by approximately 42% and the fourth by 22%. For the rectangular plate with $b/a = 1.5$, the first two frequency parameters are also strongly affected, decreasing from 0.32 to 0.17 (47%) and from 0.72 to 0.32 (56%) when d/b increases to 0.5. These results suggest that flexible boundary conditions can amplify the dynamic effect of side cracks, particularly when the low frequency modes involve substantial deformation near the cracked edge.

Table 5. Frequency parameters $(\omega a/2)\sqrt{\rho(1-\nu^2)/E}$ for S_1CS_2F square plates with vertical side cracks of various lengths at different locations.

c_x/a	d/b	Mode No.							
		1	2	3	4	5	6	7	8
0.5	0	0.80	0.88	1.33	1.62	2.06	2.13	2.19	2.56
	0.1	0.79	0.86	1.28	1.61	1.98	2.08	2.19	2.41
	0.2	0.73	0.83	1.22	1.57	1.80	2.03	2.13	2.31
	0.3	0.64	0.82	1.18	1.53	1.61	1.90	2.10	2.28
	0.4	0.56	0.81	1.11	1.43	1.55	1.82	2.07	2.27
	0.5	0.49	0.81	1.03	1.38	1.54	1.74	2.04	2.27
0.75	0.1	0.78	0.85	1.31	1.60	2.05	2.09	2.18	2.49
	0.2	0.72	0.83	1.29	1.56	1.93	2.05	2.17	2.41
	0.3	0.64	0.82	1.24	1.50	1.78	2.01	2.16	2.40
	0.4	0.57	0.81	1.14	1.45	1.73	1.97	2.16	2.39
	0.5	0.51	0.81	1.02	1.42	1.71	1.94	2.16	2.39

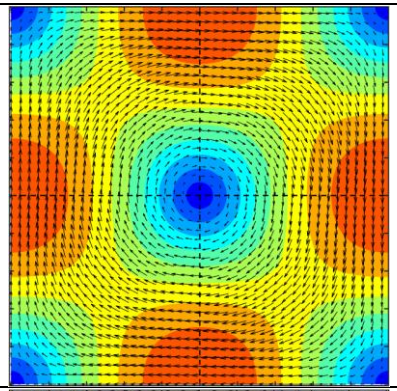
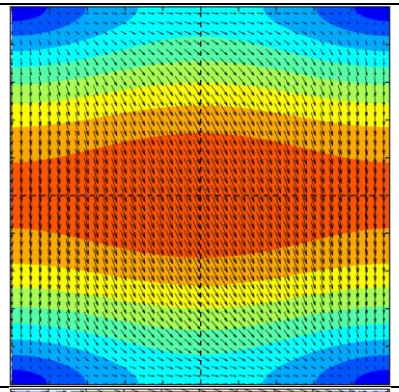
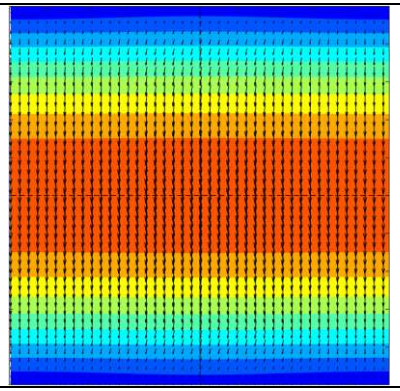
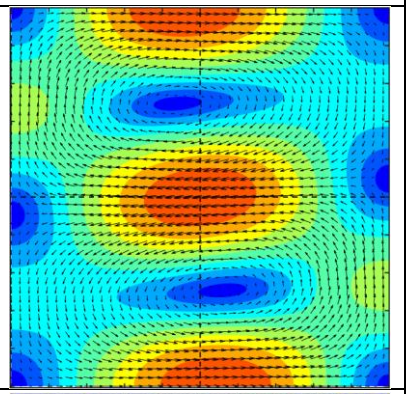
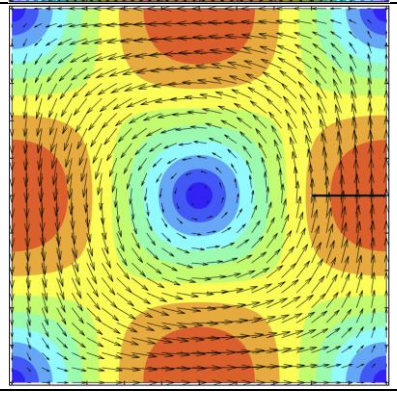
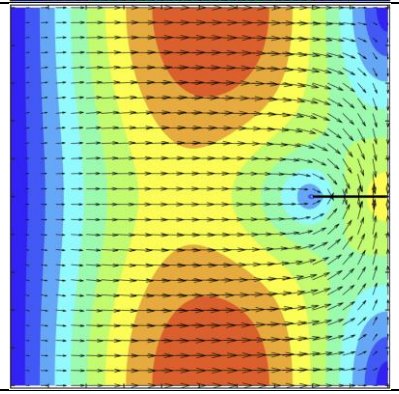
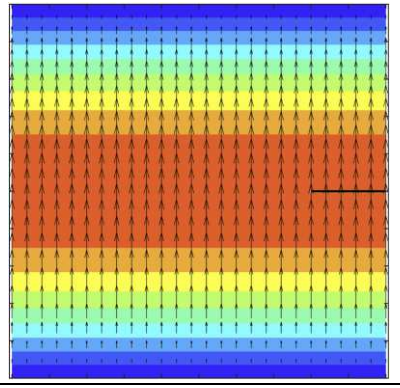
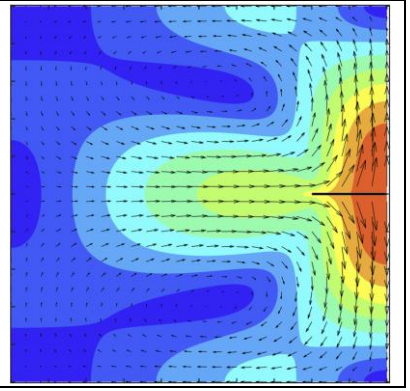
Table 6. Frequency parameters $(\omega a/2)\sqrt{\rho(1-\nu^2)/E}$ for S_2FS_1F rectangular plates with vertical side cracks of various lengths at different locations.

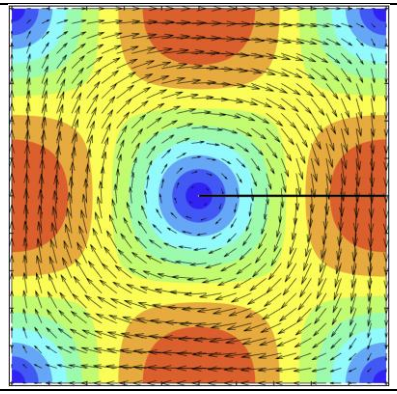
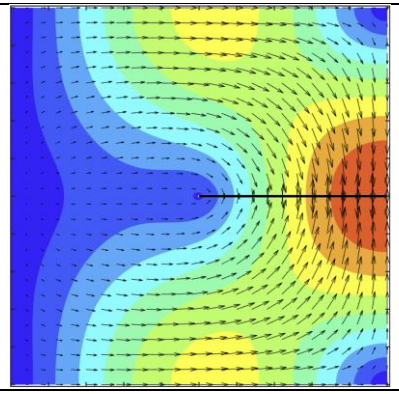
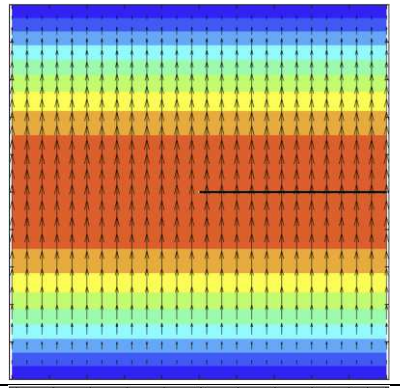
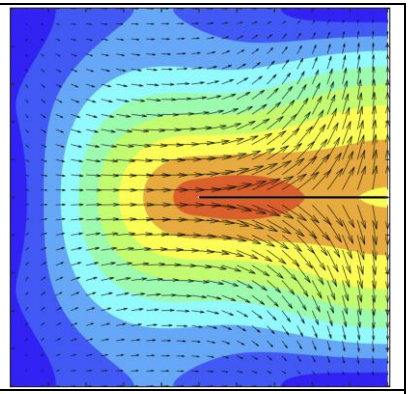
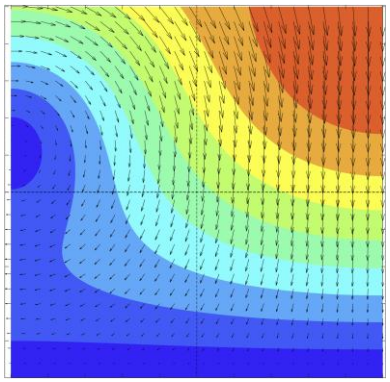
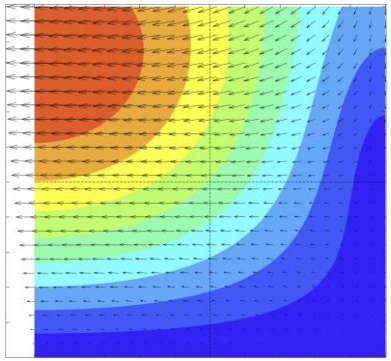
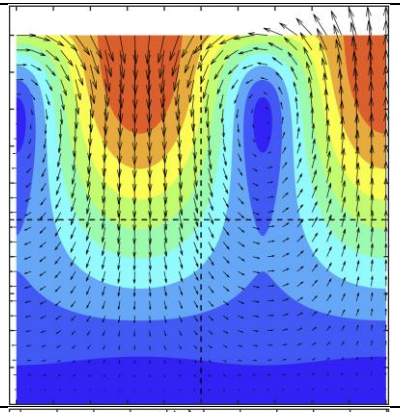
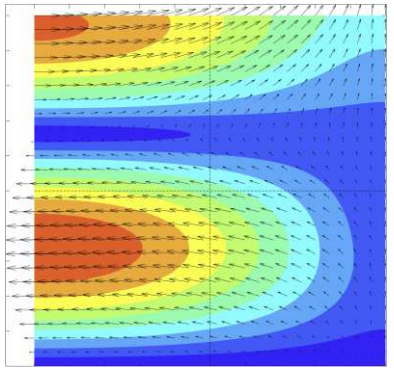
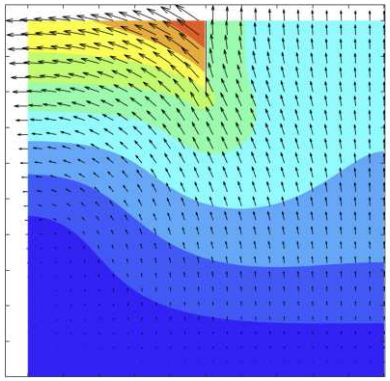
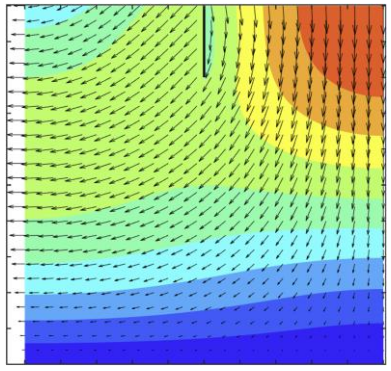
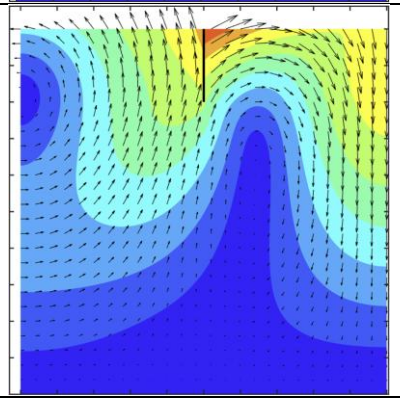
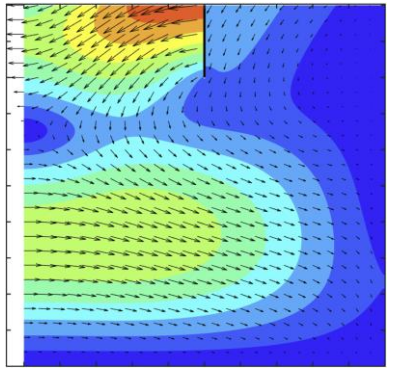
b/a	c_x/a	d/b	Mode No.							
			1	2	3	4	5	6	7	8
1	0.5	0	0.26	0.74	1.17	1.22	1.49	1.57	2.07	2.10
		0.1	0.25	0.73	1.13	1.21	1.48	1.55	1.98	2.09
		0.2	0.22	0.68	1.06	1.20	1.46	1.55	1.79	2.02
		0.3	0.19	0.62	0.99	1.19	1.45	1.55	1.60	1.87
		0.4	0.16	0.56	0.92	1.19	1.44	1.45	1.54	1.82
		0.5	0.13	0.49	0.85	1.19	1.37	1.45	1.50	1.80
	0.75	0.1	0.25	0.74	1.10	1.22	1.49	1.54	1.88	2.09
		0.2	0.24	0.71	0.96	1.20	1.43	1.51	1.66	2.02
		0.3	0.23	0.62	0.86	1.15	1.37	1.49	1.58	1.74
		0.4	0.20	0.51	0.83	1.04	1.35	1.48	1.51	1.60
		0.5	0.17	0.43	0.81	0.95	1.34	1.38	1.48	1.58
1.5	0.75	0	0.32	0.72	0.99	1.01	1.23	1.36	1.53	1.83
		0.1	0.31	0.71	0.96	1.00	1.12	1.31	1.52	1.71
		0.2	0.29	0.65	0.79	1.00	1.05	1.29	1.37	1.55
		0.3	0.26	0.50	0.75	0.99	1.02	1.17	1.31	1.42
		0.4	0.21	0.39	0.73	0.94	1.01	1.11	1.25	1.31
		0.5	0.17	0.32	0.69	0.90	1.00	1.02	1.20	1.31

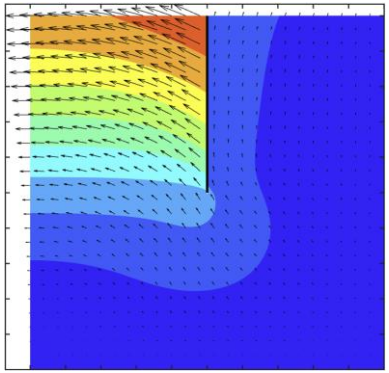
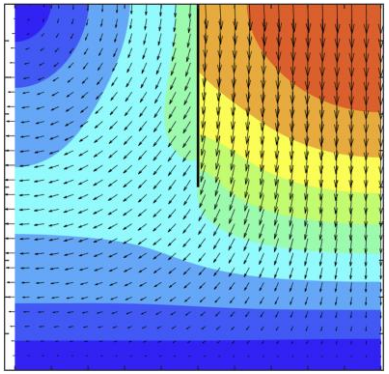
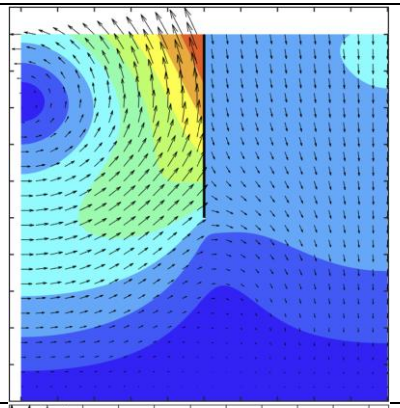
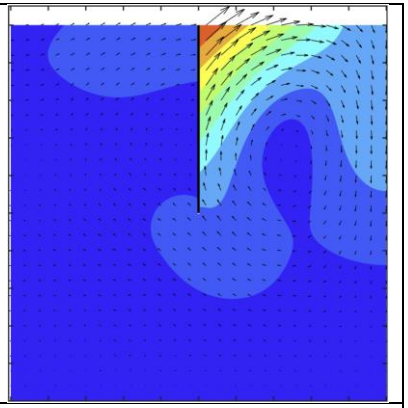
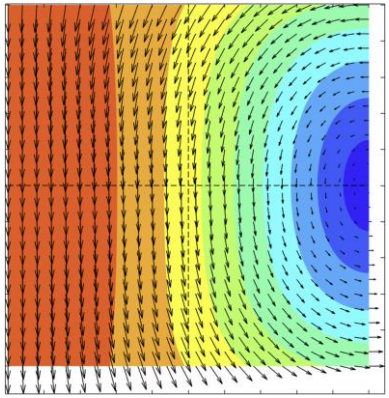
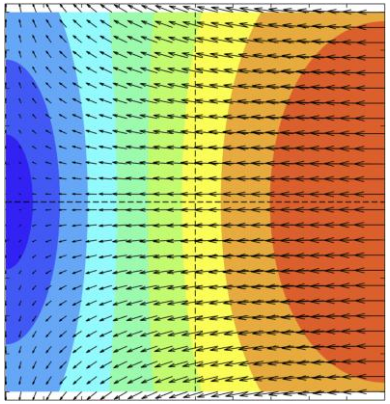
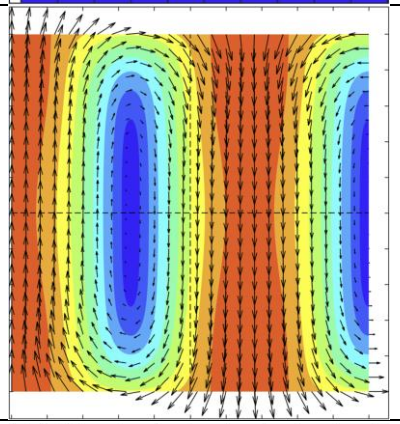
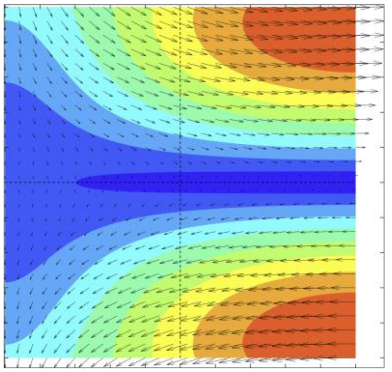
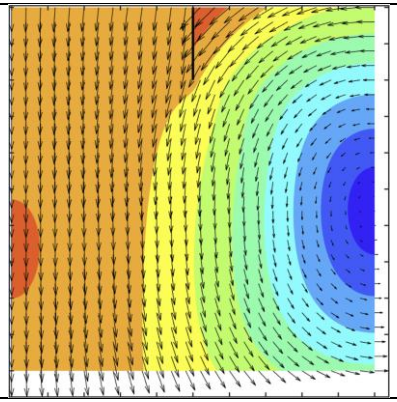
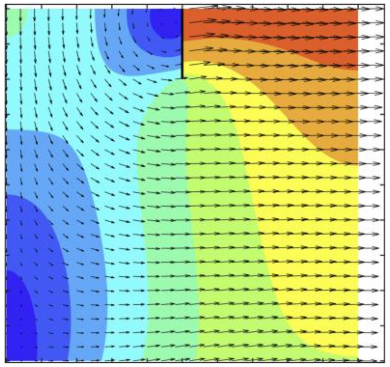
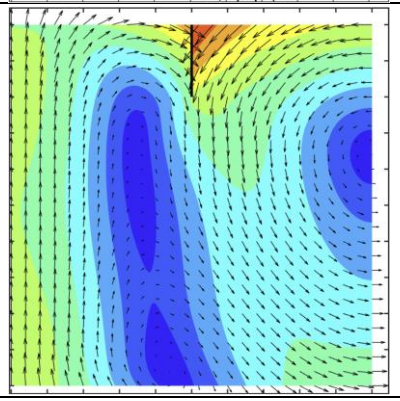
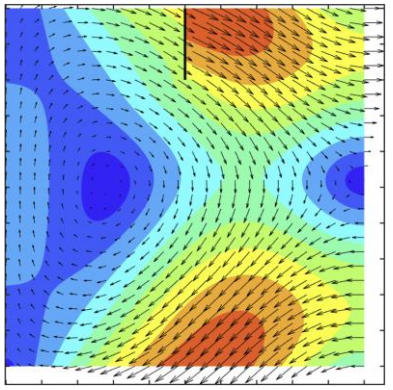
The mode shapes in Table 7 provide further physical interpretation of the frequency trends. For the intact $S_2S_2S_2S_2$ and S_2FS_1F plates, the displacement fields exhibit clear symmetry. As the crack length increases, these symmetries are broken. The vector plots clearly show a discontinuity or a jump in the displacement field across the crack faces, particularly evident in the higher modes. For $d/a = 0.5$, the crack introduces a significant disturbance, causing

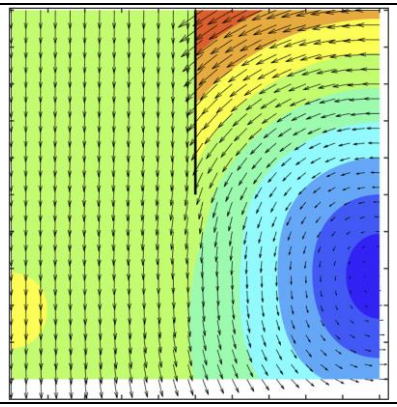
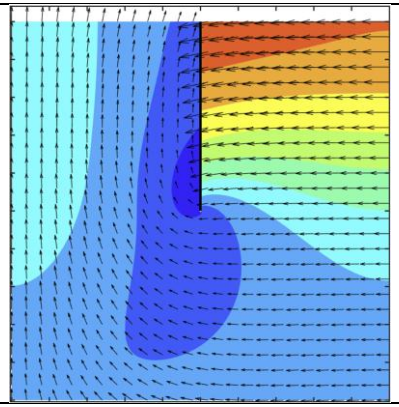
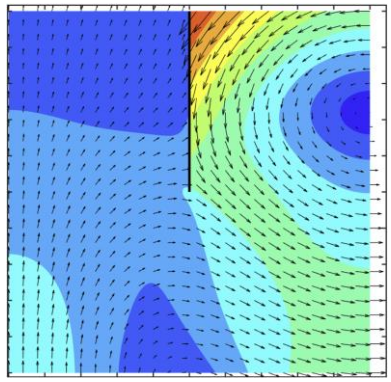
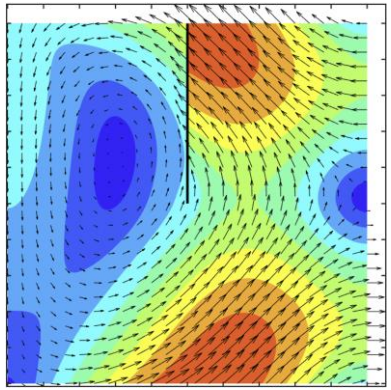
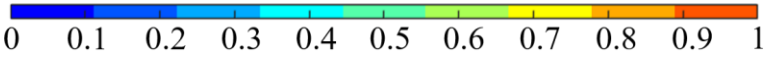
the displacement vectors to orient themselves along the crack path, which confirms the localized loss of shear and normal stiffness at the crack interface. Overall, these behaviours are consistent with the larger frequency reductions observed in Table 4 to Table 6.

Table 7. Mode shapes for $S_2S_2S_2S_2$, S_1CS_2F, and S_2FS_1F side-cracked square plates.

Boundary conditions	d/a (or d/b)	Mode No. 1	2	3	4
$S_2S_2S_2S_2$	0				
	0.2				

	0.5				
S_1CS_2F	0				
	0.2				

	0.5				
S_2FS_1F	0				
	0.2				

	0.5				
Plot legend					

4.2 Internally cracked square plates

The investigation is extended to plates containing a straight horizontal internal crack. Unlike the side-cracked cases where the domain was divided into four subdomains, the internally cracked plate is decomposed into six subdomains to accommodate the crack geometry. Table 8 to Table 10 present the first eight frequency parameters for $S_2S_2S_2S_2$, S_1CS_2F, and S_2FS_1F plates, respectively, considering both central $(x_c/a, y_c/b) = (0.5, 0.5)$ and eccentric (0.5, 0.75) crack locations.

In Table 8, for a centrally located crack, the first three frequency parameters are almost unaffected even at $d/a = 0.5$, whereas the seventh and eighth parameters drops by approximately 22% and 14%, respectively. This indicates that the lower modes of this boundary condition have limited modal strain energy in the vicinity of the central horizontal crack, while some higher modes interact more strongly with the crack. The influence of crack location is also mode dependent. For example, shifting the crack from $y_c/b = 0.5$ to $y_c/b = 0.75$ makes the second and fourth modes more sensitive, while the seventh frequency parameter remains nearly unchanged.

Table 8. Frequency parameters $(\omega a/2)\sqrt{\rho(1-\nu^2)/E}$ for $S_2S_2S_2S_2$ square plates with horizontal internal cracks of various lengths at different locations.

$\left(\frac{x_c}{a},\frac{y_c}{b}\right)$	d/a	Mode No.							
		1	2	3	4	5	6	7	8
(0.5, 0.5)	0	1.31	1.57	1.57	2.08	2.08	2.22	2.63	2.94
	0.1	1.31	1.57	1.57	2.08	2.08	2.21	2.59	2.88
	0.2	1.31	1.57	1.57	2.08	2.08	2.17	2.41	2.76
	0.3	1.31	1.57	1.57	2.07	2.07	2.09	2.16	2.64
	0.4	1.31	1.57	1.57	1.96	2.00	2.05	2.06	2.57
	0.5	1.31	1.57	1.57	1.84	1.90	2.02	2.04	2.54
(0.5, 0.75)	0.1	1.31	1.56	1.57	2.07	2.07	2.22	2.63	2.91
	0.2	1.31	1.51	1.57	2.03	2.05	2.20	2.63	2.83
	0.3	1.31	1.45	1.57	1.96	2.02	2.19	2.63	2.75
	0.4	1.31	1.38	1.57	1.86	2.00	2.17	2.63	2.69
	0.5	1.30	1.32	1.57	1.77	1.98	2.15	2.63	2.66

The influence of boundary conditions remains a dominant factor for internally cracked plates. In the S_1CS_2F plate (Table 9), which features a mix of clamped and free edges, the fundamental frequency is no longer immune to the central crack, dropping from 0.80 to 0.64 (20% reduction) as d/a reaches 0.5. For the S_2FS_1F case (Table 10), the second mode remains almost insensitive to crack growth, whereas the third to fifth modes show clear reductions for both crack locations. The seventh mode is especially affected by the off-centre crack, decreasing from 2.07 to 1.64 (21% reduction) at $d/a = 0.5$.

Table 9. Frequency parameters $(\omega a/2)\sqrt{\rho(1-\nu^2)/E}$ for S_1CS_2F square plates with horizontal internal cracks of various lengths at different locations.

$\left(\frac{x_c}{a},\frac{y_c}{b}\right)$	d/a	Mode No.							
		1	2	3	4	5	6	7	8
(0.5, 0.5)	0	0.80	0.88	1.33	1.62	2.06	2.13	2.19	2.56
	0.1	0.79	0.88	1.32	1.61	2.06	2.13	2.18	2.54
	0.2	0.77	0.88	1.30	1.60	2.03	2.09	2.15	2.47
	0.3	0.74	0.87	1.26	1.57	1.93	2.07	2.13	2.38
	0.4	0.69	0.87	1.22	1.53	1.84	2.05	2.11	2.31
	0.5	0.64	0.86	1.18	1.48	1.77	2.03	2.09	2.25
(0.5, 0.75)	0.1	0.80	0.88	1.32	1.61	2.05	2.12	2.17	2.53
	0.2	0.79	0.88	1.29	1.58	1.92	2.07	2.11	2.43
	0.3	0.77	0.88	1.24	1.51	1.69	2.01	2.08	2.35
	0.4	0.74	0.87	1.15	1.39	1.58	1.95	2.05	2.31
	0.5	0.69	0.87	1.06	1.28	1.53	1.89	1.99	2.26

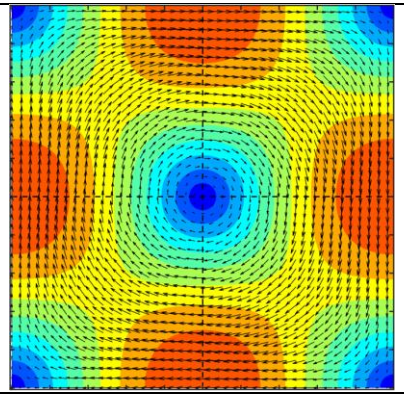
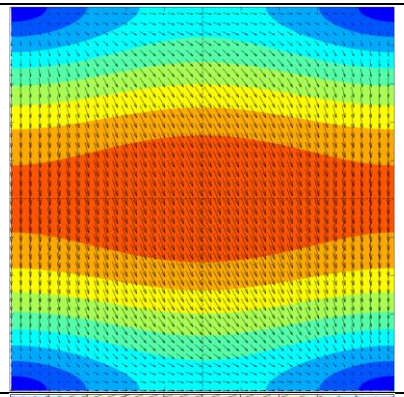
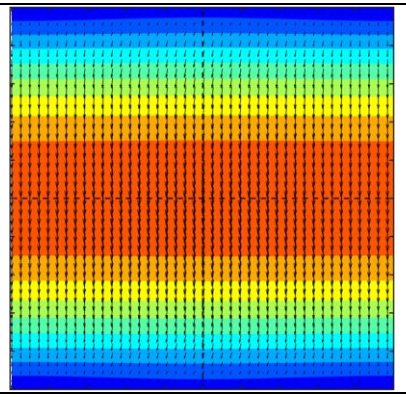
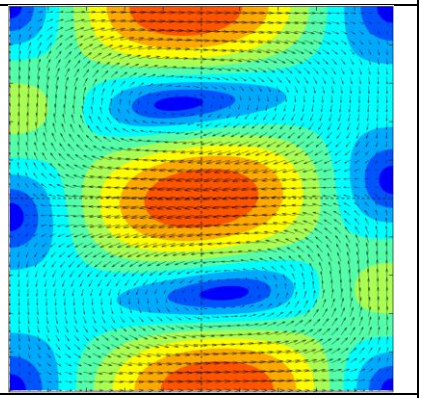
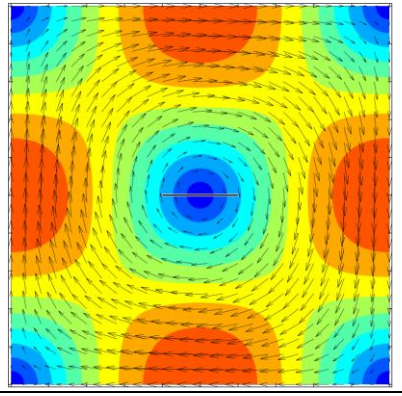
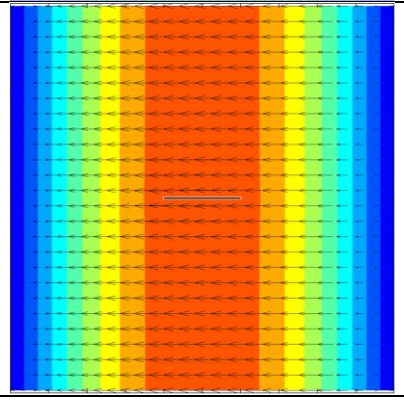
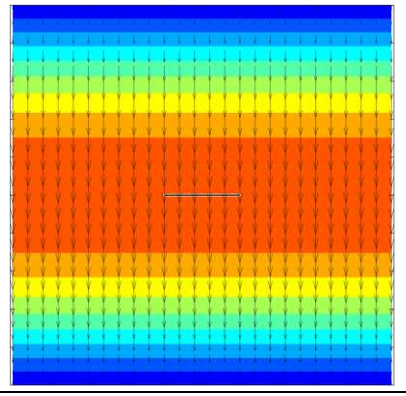
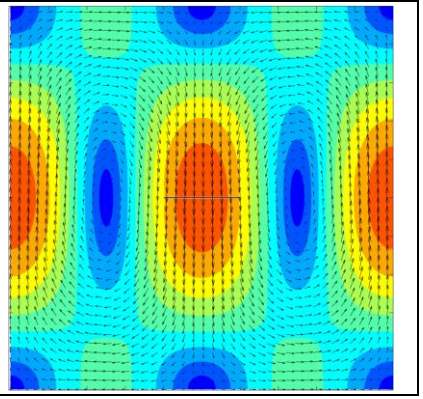
Table 10. Frequency parameters $(\omega a/2)\sqrt{\rho(1-\nu^2)/E}$ for S_2FS_1F square plates with horizontal internal cracks of various lengths at different locations.

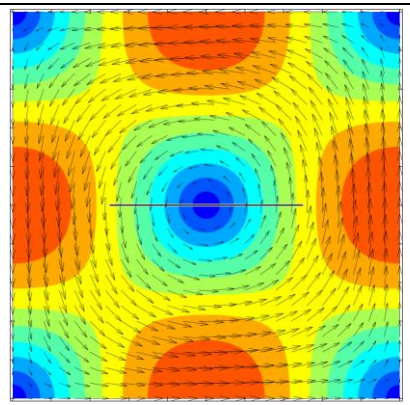
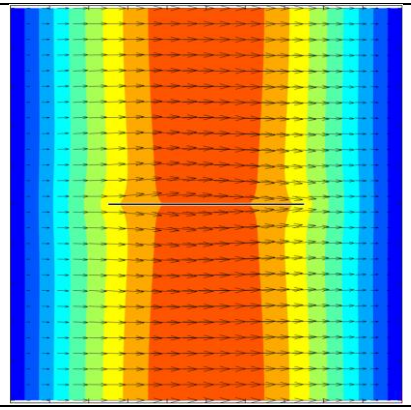
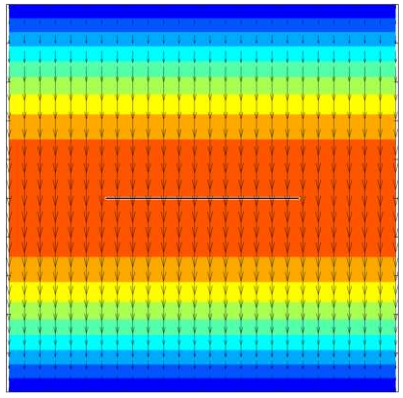
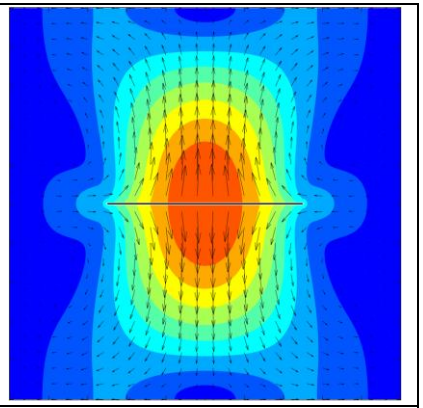
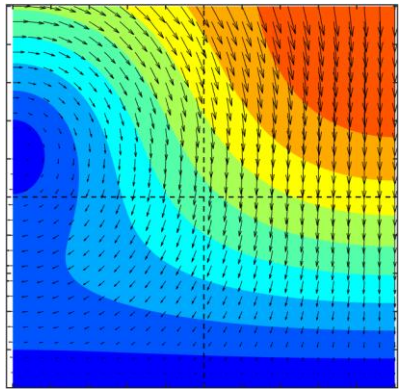
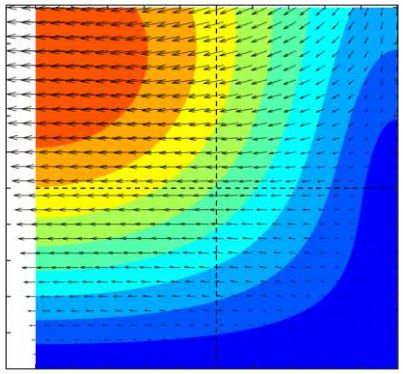
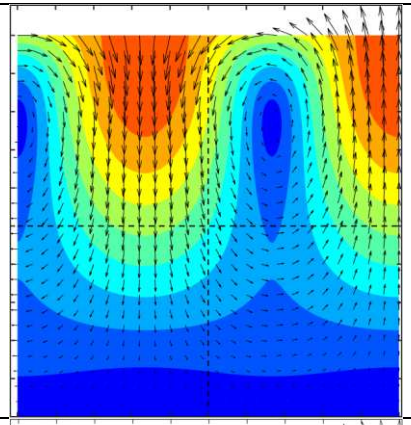
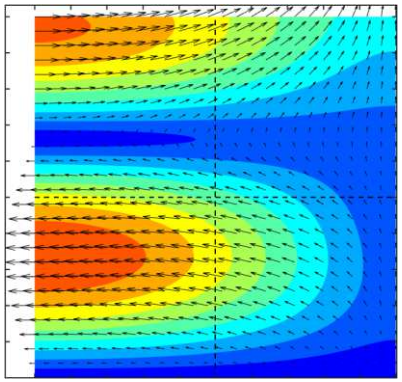
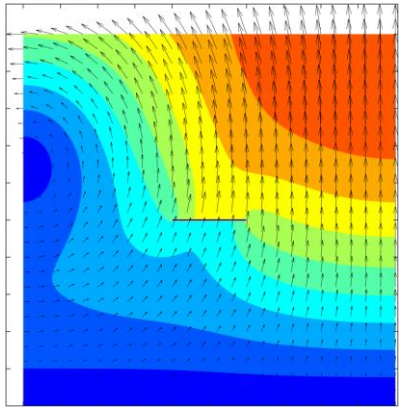
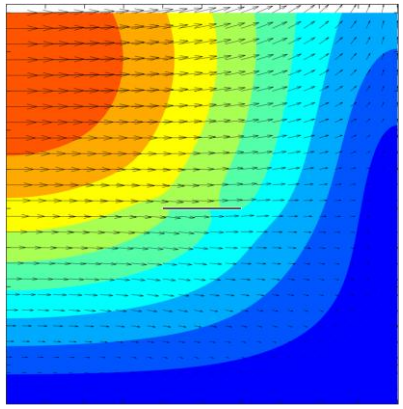
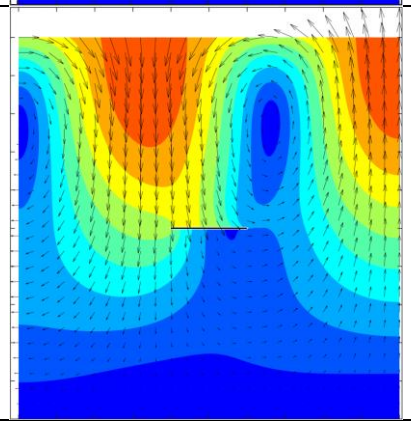
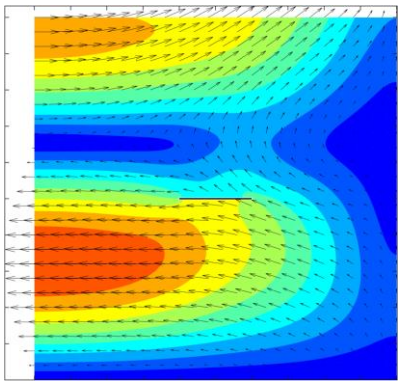
$\left(\frac{x_c}{a},\frac{y_c}{b}\right)$	d/a	Mode No.							
		1	2	3	4	5	6	7	8
(0.5, 0.5)	0	0.26	0.74	1.17	1.22	1.49	1.57	2.07	2.10
	0.1	0.26	0.74	1.16	1.22	1.46	1.56	2.07	2.09
	0.2	0.25	0.74	1.14	1.21	1.36	1.55	2.05	2.08
	0.3	0.25	0.74	1.11	1.20	1.21	1.54	2.02	2.06
	0.4	0.25	0.74	1.05	1.06	1.19	1.52	1.99	2.05

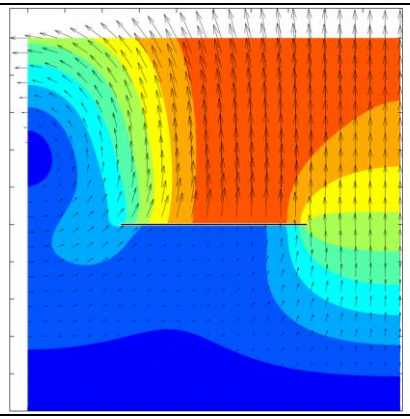
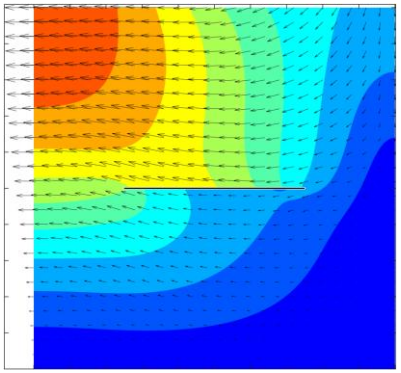
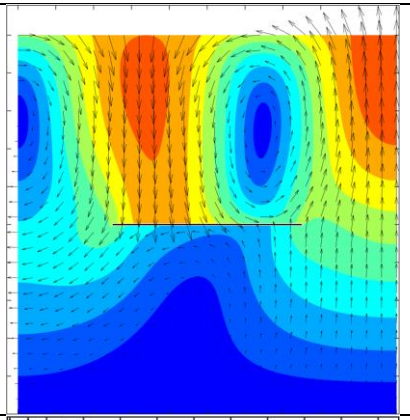
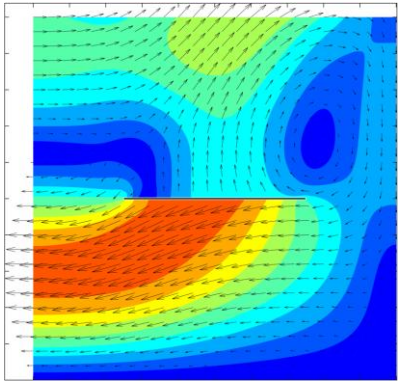
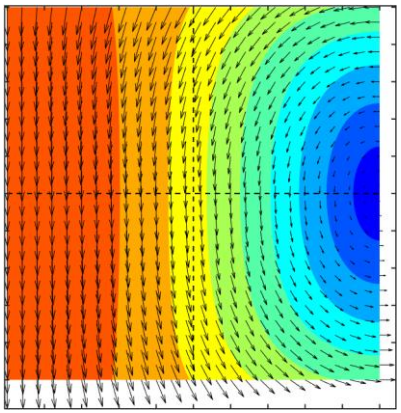
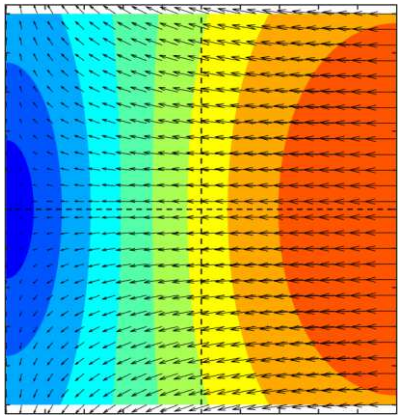
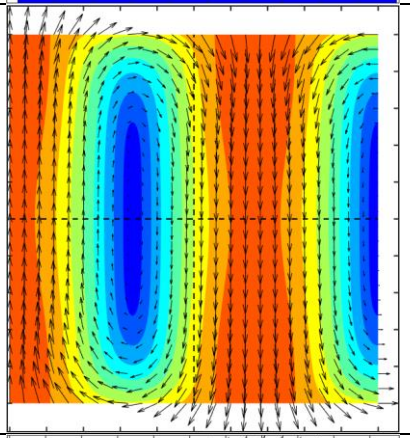
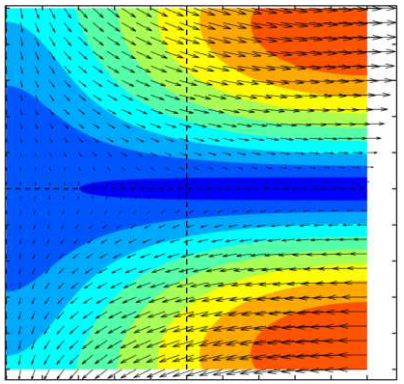
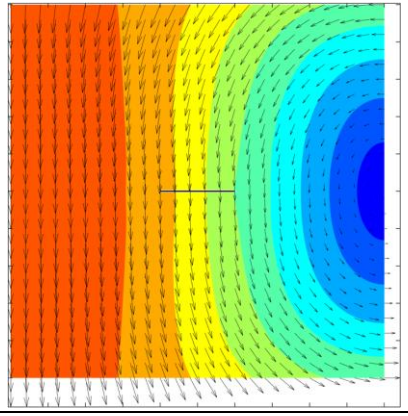
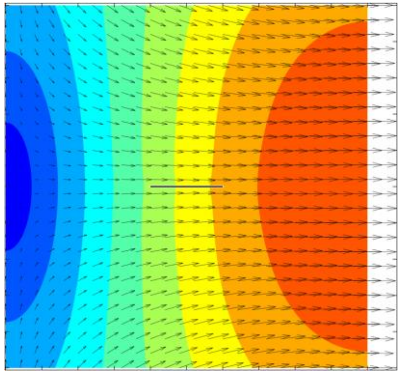
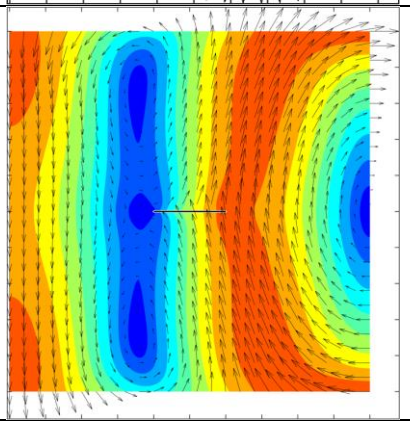
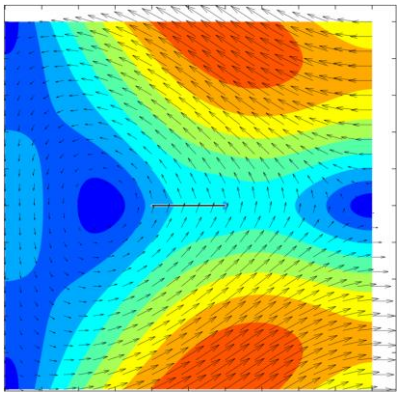
	0.5	0.24	0.73	0.92	1.01	1.18	1.48	1.96	2.03
(0.5, 0.75)	0.1	0.26	0.74	1.16	1.22	1.48	1.56	2.06	2.09
	0.2	0.26	0.74	1.15	1.21	1.41	1.55	1.96	2.08
	0.3	0.25	0.74	1.12	1.20	1.28	1.54	1.82	2.06
	0.4	0.25	0.74	1.03	1.11	1.21	1.53	1.72	2.01
	0.5	0.25	0.74	0.88	1.05	1.20	1.50	1.64	1.97

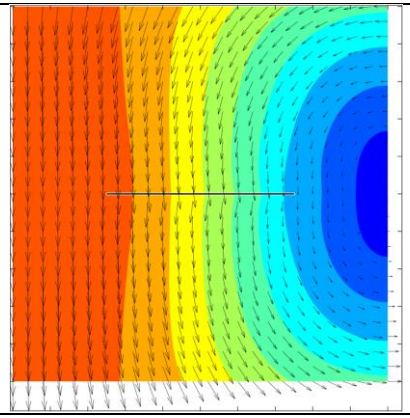
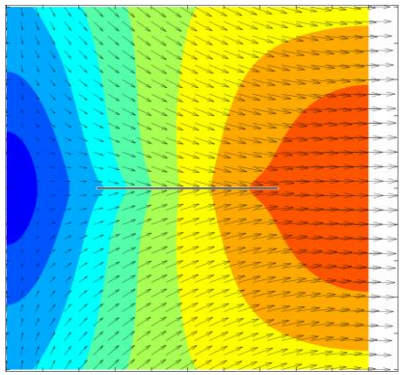
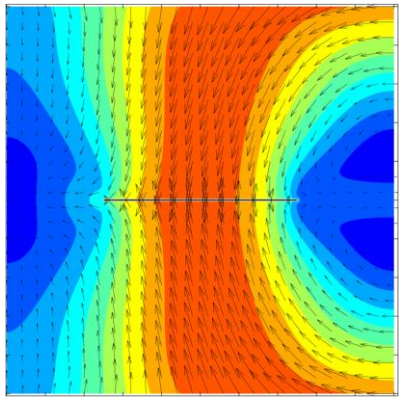
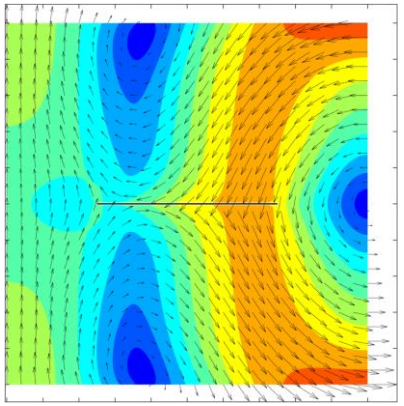
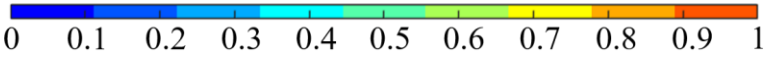
Table 11 provides a visual confirmation of the numerical trends in frequency parameters. For short cracks, the global displacement patterns remain close to those of the intact plate, although a local discontinuity can appear along the crack faces. As the crack length increases, the displacement jump becomes more pronounced and the vector field is locally redirected around the crack tips. The centrally cracked $S_2S_2S_2S_2$ plate retains a relatively regular modal pattern in the first few modes, consistent with the small frequency reductions observed in Table 8. In contrast, the S_1CS_2F and S_2FS_1F plates exhibit stronger local distortion and a more evident redistribution of the displacement field, which agrees with the larger frequency reductions reported in Table 9 and Table 10. Overall, the internal-crack results confirm that the proposed Fourier series formulation can capture both the global frequency reduction and the local modal disturbance introduced by a straight through crack.

Table 11. Mode shapes for $S_2S_2S_2S_2$, S_1CS_2F, and S_2FS_1F square plates with central internal cracks.

Boundary conditions	d/a	Mode No.			
		1	2	3	4
$S_2S_2S_2S_2$	0				
	0.2				

	0.5				
S_1CS_2F	0				
	0.2				

	0.5				
S_2FS_1F	0				
	0.2				

	0.5				
Plot legend					

5 Conclusions

This study has established an analytical-type Fourier series formulation for the free in-plane vibration of isotropic rectangular plates with a straight through side crack or internal crack, and has used it to obtain frequency parameters and mode shapes across a range of crack and boundary configurations. The principal conclusions are as follows:

1. For intact plates, the frequency parameters converge rapidly, with changes beyond $M = N = 10$ confined to the third decimal place, and agree with the published exact, Ritz, and superposition solutions to at least three significant figures across all boundary conditions and modes considered.
2. For side-cracked and internally cracked plates, the leading two decimal places are essentially settled by $M = N = 10$, and the residual change between $M = N = 20$ and 22 remains within 0.001. The converged frequency parameters agree closely with finite element results across all plate configurations examined. Because the supplemented cosine series can be differentiated term by term, as the truncation numbers increase, the governing equations and all continuity, boundary, and crack face conditions are satisfied with increasing accuracy. The solution can therefore, in principle, be refined to any prescribed accuracy.

3. Convergence is not one-sided: the frequency parameters of intact plates approach the converged value monotonically from above, whereas individual modes of the cracked plate may approach from above or below. The present results are therefore not rigorous bounds, but convergence is rapid and stable in every case considered.
4. A truncation of $M = N = 20$ has been adopted for the parametric study in Section 4, producing the reported frequency parameters to two decimal places while keeping the problem computationally efficient, a consideration that is particularly important for the six-subdomain model of an internally cracked plate.
5. Crack-induced frequency reductions are strongly mode- and boundary condition-dependent. Introducing a crack either decreases or leaves unchanged the ordered natural frequencies. For an $S_2S_2S_2S_2$ square plate with a horizontal side crack at mid-height, the first and third frequency parameters are essentially unaffected up to $d/a = 0.5$, while the fourth, seventh, and eighth fall by approximately 19%, 14%, and 22%, respectively. Plates with clamped or free edges are significantly more sensitive than fully S_2-supported plates: the first frequency of an S_1CS_2F plate falls by about 39% for a vertical side crack at $d/b = 0.5$, and the S_2FS_1F configuration shows the largest reductions of the cases considered, with the first two frequency parameters of a $b/a = 1.5$ plate falling by 47% and 56% at $d/b = 0.5$.
6. Internal cracks produce similar but generally smaller reductions in the lower modes, while crack location can alter the sensitivity of individual modes. For an $S_2S_2S_2S_2$ plate with a central horizontal internal crack, the first three frequency parameters remain essentially unchanged up to $d/a = 0.5$, while the seventh and eighth decrease by about 22% and 14%. Moving the crack away from the centre increases the sensitivity of some modes but reduces that of others. For example, the second and fourth modes of the $S_2S_2S_2S_2$ plate become more sensitive, whereas the seventh is largely unaffected; in the S_2FS_1F plate, the seventh mode shows its largest reduction when the crack is offset, decreasing from 2.07 to 1.64 (about 21%). The mode shapes support these observations by showing increasingly pronounced displacement discontinuities and stronger local redistribution as the crack length increases, particularly for modes exhibiting larger frequency reductions.

The present results provide benchmark in-plane frequency parameters and mode shapes for rectangular plates with straight through cracks where analytical-type data were previously unavailable. The formulation may be extended to other cracked or cutout plate configurations that can be represented

by assemblies of rectangular subdomains. It may also be applied to orthotropic or laminated plates, multiple or inclined cracks, and elastically restrained edges, which are left for future work.

Appendix A. Fourier coefficients used in the formulation

The Fourier coefficients used in Eq. (10) are obtained from the auxiliary functions defined in Eq. (6). For compactness, the derivation is first given for a generic interval $0 \le z \le L$, with $\zeta = z/L$ and $k_m = m\pi/L$. The two auxiliary functions are

$$\begin{aligned} \chi_1(z) &= L\zeta(\zeta-1)^2 \\ \chi_2(z) &= L\zeta^2(\zeta-1) \end{aligned} \tag{A.1}$$

The corresponding Fourier cosine coefficients are defined by

$$\begin{aligned} \chi_r(z) &= \sum_{m=0}^{M} A_{rm}^{\chi} \cos k_m z \\ \frac{d\chi_r(z)}{dz} &= \sum_{m=0}^{M} A_{rm}^{\chi'} \cos k_m z \\ \frac{d^2\chi_r(z)}{dz^2} &= \sum_{m=0}^{M} A_{rm}^{\chi''} \cos k_m z \end{aligned} \tag{A.2}$$

where $r = 1,2$. The coefficients are calculated from

$$\begin{aligned} A_{rm}^{\chi} &= \frac{\varepsilon_m}{L}\int_0^L \chi_r(z)\cos k_m z\, dz \\ A_{rm}^{\chi'} &= \frac{\varepsilon_m}{L}\int_0^L \frac{d\chi_r(z)}{dz}\cos k_m z\, dz \\ A_{rm}^{\chi''} &= \frac{\varepsilon_m}{L}\int_0^L \frac{d^2\chi_r(z)}{dz^2}\cos k_m z\, dz \end{aligned} \tag{A.3}$$

with $\varepsilon_0 = 1$ and $\varepsilon_m = 2$ when $m \ge 1$.

For $m = 0$, the coefficients are

$$A_{10}^{\chi} = \frac{L}{12}, \qquad A_{20}^{\chi} = -\frac{L}{12}$$
$$A_{10}^{\chi'} = 0, \qquad A_{20}^{\chi'} = 0 \tag{A.4}$$
$$A_{10}^{\chi''} = -\frac{1}{L}, \qquad A_{20}^{\chi''} = \frac{1}{L}$$

For $m \geq 1$, the coefficients are

$$A_{1m}^{\chi} = \frac{2L}{\pi^4 m^4}[-6(-1)^m - \pi^2 m^2 + 6], \quad A_{2m}^{\chi} = \frac{2L}{\pi^4 m^4}[(-1)^m \pi^2 m^2 - 6(-1)^m + 6]$$
$$A_{1m}^{\chi'} = \frac{4}{\pi^2 m^2}[(-1)^m + 2], \quad A_{2m}^{\chi'} = \frac{4}{\pi^2 m^2}[2(-1)^m + 1] \tag{A.5}$$
$$A_{1m}^{\chi''} = \frac{12}{L\pi^2 m^2}[(-1)^m - 1], \quad A_{2m}^{\chi''} = \frac{12}{L\pi^2 m^2}[(-1)^m - 1]$$

Therefore, for the x_j-direction auxiliary functions,

$$\alpha_{rm}^{(j)} = A_{rm}^{\chi}|_{L=a_j}, \qquad \hat{\alpha}_{rm}^{(j)} = A_{rm}^{\chi'}|_{L=a_j}, \qquad \tilde{\alpha}_{rm}^{(j)} = A_{rm}^{\chi''}|_{L=a_j} \tag{A.6}$$

Similarly, for the y_j-direction auxiliary functions,

$$\gamma_{rn}^{(j)} = A_{rn}^{\chi}|_{L=b_j}, \qquad \hat{\gamma}_{rn}^{(j)} = A_{rn}^{\chi'}|_{L=b_j}, \qquad \tilde{\gamma}_{rn}^{(j)} = A_{rn}^{\chi''}|_{L=b_j} \tag{A.7}$$

The sine functions generated by the mixed derivatives are also expanded into Fourier cosine series. For a generic interval $0 \leq z \leq L$,

$$\sin\frac{p\pi z}{L} = \sum_{m=0}^{M} S_{pm} \cos\frac{m\pi z}{L} \tag{A.8}$$

where

$$S_{pm} = \frac{\varepsilon_m}{L}\int_0^L \sin\frac{p\pi z}{L}\cos\frac{m\pi z}{L}\, dz \tag{A.9}$$

For $p = 0$, $S_{0m} = 0$. For $p \geq 1$, the coefficient is

$$S_{pm}=\begin{cases}\dfrac{\varepsilon_m p[(-1)^{p+m}-1]}{\pi(m^2-p^2)}, & m\neq p\\ 0, & m=p\end{cases} \tag{A.10}$$

Accordingly, $S_{pm}^{x(j)}=S_{pm}$ with $z=x_j$ and $L=a_j$, and $S_{qn}^{y(j)}=S_{qn}$ with $z=y_j$ and $L=b_j$.

Appendix B. Continuity conditions for a horizontal interconnection boundary

For the horizontal interconnection boundary, consider the interface between the top edge of subdomain 3 and the bottom edge of subdomain 4 in Fig. 1(b) as an example, the displacement continuity condition for u gives

$$\alpha_{1m}^{(3)}\sum_{n=0}^{N}(-1)^n c_n^{(3)}+\alpha_{2m}^{(3)}\sum_{n=0}^{N}(-1)^n d_n^{(3)}-\alpha_{1m}^{(4)}\sum_{n=0}^{N}c_n^{(4)}-\alpha_{2m}^{(4)}\sum_{n=0}^{N}d_n^{(4)}=-\sum_{n=0}^{N}(-1)^n A_{mn}^{(3)}+\sum_{n=0}^{N}A_{mn}^{(4)},\qquad m=0,1,\dots,M \tag{B.1}$$

The displacement continuity condition for v gives

$$\alpha_{1m}^{(3)}\sum_{n=0}^{N}(-1)^n g_n^{(3)}+\alpha_{2m}^{(3)}\sum_{n=0}^{N}(-1)^n h_n^{(3)}-\alpha_{1m}^{(4)}\sum_{n=0}^{N}g_n^{(4)}-\alpha_{2m}^{(4)}\sum_{n=0}^{N}h_n^{(4)}=-\sum_{n=0}^{N}(-1)^n B_{mn}^{(3)}+\sum_{n=0}^{N}B_{mn}^{(4)},\qquad m=0,1,\dots,M \tag{B.2}$$

The normal traction continuity condition gives

$$\begin{aligned}&f_m^{(3)}-e_m^{(4)}+\nu\left[\hat{\alpha}_{1m}^{(3)}\sum_{n=0}^{N}(-1)^n c_n^{(3)}+\hat{\alpha}_{2m}^{(3)}\sum_{n=0}^{N}(-1)^n d_n^{(3)}-\hat{\alpha}_{1m}^{(4)}\sum_{n=0}^{N}c_n^{(4)}-\hat{\alpha}_{2m}^{(4)}\sum_{n=0}^{N}d_n^{(4)}\right]\\&=\nu\left[\sum_{p=0}^{M}\sum_{n=0}^{N}(-1)^n A_{pn}^{(3)}\lambda_p^{(3)}S_{pm}^{x(3)}-\sum_{p=0}^{M}\sum_{n=0}^{N}A_{pn}^{(4)}\lambda_p^{(4)}S_{pm}^{x(4)}\right],\quad m=0,1,\dots,M\end{aligned} \tag{B.3}$$

The shear traction continuity condition gives

$$b_m^{(3)} - a_m^{(4)} + \hat{\alpha}_{1m}^{(3)} \sum_{n=0}^{N} (-1)^n g_n^{(3)} + \hat{\alpha}_{2m}^{(3)} \sum_{n=0}^{N} (-1)^n h_n^{(3)} - \hat{\alpha}_{1m}^{(4)} \sum_{n=0}^{N} g_n^{(4)} - \hat{\alpha}_{2m}^{(4)} \sum_{n=0}^{N} h_n^{(4)}$$
$$= \sum_{p=0}^{M} \sum_{n=0}^{N} (-1)^n B_{pn}^{(3)} \lambda_p^{(3)} S_{pm}^{x(3)} - \sum_{p=0}^{M} \sum_{n=0}^{N} B_{pn}^{(4)} \lambda_p^{(4)} S_{pm}^{x(4)}, \quad m = 0,1,\dots,M \tag{B.4}$$

Equations (B.1)-(B.4) provide $4(M+1)$ algebraic equations for a horizontal interconnection boundary.

Appendix C. Examples of boundary conditions

Consider the traction-free conditions along the top edge of subdomain 2 in Fig. 1(a). Since this is a horizontal edge, the traction-free conditions are $\sigma_y^{(2)} = 0$ and $\tau_{xy}^{(2)} = 0$ at $y_2 = b_2$. Using Eq. (2), these conditions can be written as

$$\left(\nu \frac{\partial u^{(2)}}{\partial x_2} + \frac{\partial v^{(2)}}{\partial y_2} \right)_{y_2 = b_2} = 0 \tag{C.1}$$

and

$$\left(\frac{\partial u^{(2)}}{\partial y_2} + \frac{\partial v^{(2)}}{\partial x_2} \right)_{y_2 = b_2} = 0 \tag{C.2}$$

Substituting Eqs. (4)-(5) into Eq. (C.1), expanding the sine terms into Fourier cosine series, and collecting the coefficients of $\cos\lambda_m^{(2)} x_2$ gives

$$f_m^{(2)} + \nu \left[\hat{\alpha}_{1m}^{(2)} \sum_{n=0}^{N} (-1)^n c_n^{(2)} + \hat{\alpha}_{2m}^{(2)} \sum_{n=0}^{N} (-1)^n d_n^{(2)} \right] = \nu \sum_{p=0}^{M} \sum_{n=0}^{N} (-1)^n A_{pn}^{(2)} \lambda_p^{(2)} S_{pm}^{x(2)}, \qquad m = 0,1,\dots,M \tag{C.3}$$

Similarly, substituting Eqs. (4)-(5) into Eq. (C.2) gives

$$b_m^{(2)} + \hat{\alpha}_{1m}^{(2)} \sum_{n=0}^{N} (-1)^n g_n^{(2)} + \hat{\alpha}_{2m}^{(2)} \sum_{n=0}^{N} (-1)^n h_n^{(2)} = \sum_{p=0}^{M} \sum_{n=0}^{N} (-1)^n B_{pn}^{(2)} \lambda_p^{(2)} S_{pm}^{x(2)}, \qquad m = 0,1,\dots,M \tag{C.4}$$

Equations (C.3)-(C.4) provide $2(M+1)$ algebraic equations for the traction-free horizontal edge.

When the left boundary of subdomain 1 in Fig. 1(a) is clamped, the boundary conditions are $u^{(1)} = 0$ and $v^{(1)} = 0$ at $x_1 = 0$. Substituting Eqs. (4)-(5) into the condition $u^{(1)} = 0$, expanding the auxiliary functions into Fourier cosine series, and collecting the coefficients of $\cos\beta_n^{(1)} y_1$ gives

$$\gamma_{1n}^{(1)} \sum_{m=0}^{M} a_m^{(1)} + \gamma_{2n}^{(1)} \sum_{m=0}^{M} b_m^{(1)} = -\sum_{m=0}^{M} A_{mn}^{(1)}, \qquad n = 0,1,\dots,N \tag{C.5}$$

The condition $v^{(1)} = 0$ gives

$$\gamma_{1n}^{(1)} \sum_{m=0}^{M} e_m^{(1)} + \gamma_{2n}^{(1)} \sum_{m=0}^{M} f_m^{(1)} = -\sum_{m=0}^{M} B_{mn}^{(1)}, \qquad n = 0,1,\dots,N \tag{C.6}$$

Equations (C.5)-(C.6) provide $2(N+1)$ algebraic equations for the clamped vertical edge.

When the left boundary of subdomain 1 in Fig. 1(a) is simply supported, two definitions may be used, as described in Section 2.3. If the normal displacement is restrained and the tangential traction is zero, then $u^{(1)} = 0$ and $\tau_{xy}^{(1)} = 0$ at $x_1 = 0$. The displacement condition $u^{(1)} = 0$ gives the same equation as Eq. (C.5). The shear traction condition $\tau_{xy}^{(1)} = 0$ gives

$$g_n^{(1)} + \hat{\gamma}_{1n}^{(1)} \sum_{m=0}^{M} a_m^{(1)} + \hat{\gamma}_{2n}^{(1)} \sum_{m=0}^{M} b_m^{(1)} = \sum_{m=0}^{M} \sum_{q=0}^{N} A_{mq}^{(1)} \beta_q^{(1)} S_{qn}^{y(1)}, \qquad n = 0,1,\dots,N \tag{C.7}$$

Alternatively, if the tangential displacement is restrained and the normal traction is zero, then $v^{(1)} = 0$ and $\sigma_x^{(1)} = 0$ at $x_1 = 0$. The displacement condition $v^{(1)} = 0$ gives the same equation as Eq. (C.6). The normal traction condition $\sigma_x^{(1)} = 0$ gives

$$c_n^{(1)} + \nu \left[\hat{\gamma}_{1n}^{(1)} \sum_{m=0}^{M} e_m^{(1)} + \hat{\gamma}_{2n}^{(1)} \sum_{m=0}^{M} f_m^{(1)} \right] = \nu \sum_{m=0}^{M} \sum_{q=0}^{N} B_{mq}^{(1)} \beta_q^{(1)} S_{qn}^{y(1)}, \qquad n = 0,1,\dots,N \tag{C.8}$$

In total, the in-plane simply supported vertical edge provides $2(N+1)$ algebraic equations.

The above equations are examples only. The boundary conditions on other vertical and horizontal edges can be obtained in the same manner by substituting the corresponding edge coordinate, using the appropriate edge values of the auxiliary functions, and collecting the coefficients of the relevant Fourier cosine basis.

Acknowledgements

None.

Funding Declaration

This research did not receive any specific grant from funding agencies in the public, commercial, or not-for-profit sectors.

Statements and Declarations

The author(s) declared no potential conflicts of interest with respect to the research, authorship, and/or publication of this article.

Data Availability

The data that support the findings of this study are available from the corresponding author upon reasonable request.

References

Bachene M., Tiberkak R., Rechak S. (2009). Vibration analysis of cracked plates using the extended finite element method. Arch. Appl. Mech. **79**(3): 249-262. https://doi.org/10.1007/s00419-008-0224-7

Bardell N. S., Langley R. S., Dunsdon J. M. (1996). On the free in-plane vibration of isotropic rectangular plates. J. Sound Vib. **191**(3): 459-467. https://doi.org/10.1006/jsvi.1996.0134

Bercin A. N. (1996). An assessment of the effects of in-plane vibrations on the energy flow between coupled plates. J. Sound Vib. **191**(5): 661-680. https://doi.org/10.1006/jsvi.1996.0149

Chen J.-S. (1996). Vibration and stability of a spinning disk under stationary distributed edge loads. J. Appl. Mech. **63**(2): 439-444. https://doi.org/10.1115/1.2788886
Chen J.-S., Jhu J.-L. (1996). In-plane response of a rotating annular disk under fixed concentrated edge loads. Int. J. Mech. Sci. **38**(12): 1285-1293. https://doi.org/10.1016/0020-7403(96)00002-1
Chen Y., An D., Zhou C., Li Y., Xu J., Li R. (2023). Analytical free vibration solutions of rectangular edge-cracked plates by the finite integral transform method. Int. J. Mech. Sci. **243**: 108032. https://doi.org/10.1016/j.ijmecsci.2022.108032
Dozio L. (2010). Free in-plane vibration analysis of rectangular plates with arbitrary elastic boundaries. Mech. Res. Commun. **37**(7): 627-635. https://doi.org/10.1016/j.mechrescom.2010.09.003
Dozio L. (2011). In-plane free vibrations of single-layer and symmetrically laminated rectangular composite plates. Compos. Struct. **93**(7): 1787-1800. https://doi.org/10.1016/j.compstruct.2011.01.021
Du J., Li W. L., Jin G., Yang T., Liu Z. (2007). An analytical method for the in-plane vibration analysis of rectangular plates with elastically restrained edges. J. Sound Vib. **306**(3): 908-927. https://doi.org/10.1016/j.jsv.2007.06.011
Farag N. H., Pan J. (1999). Modal characteristics of in-plane vibration of rectangular plates. The Journal of the Acoustical Society of America **105**(6): 3295-3310. https://doi.org/10.1121/1.424658
Gorman D. J. (2004). Accurate analytical type solutions for the free in-plane vibration of clamped and simply supported rectangular plates. J. Sound Vib. **276**(1): 311-333. https://doi.org/10.1016/j.jsv.2003.07.037
Gorman D. J. (2004). Free in-plane vibration analysis of rectangular plates by the method of superposition. J. Sound Vib. **272**(3): 831-851. https://doi.org/10.1016/S0022-460X(03)00421-8
Gorman D. J. (2005). Free in-plane vibration analysis of rectangular plates with elastic support normal to the boundaries. J. Sound Vib. **285**(4): 941-966. https://doi.org/10.1016/j.jsv.2004.09.017
Gorman D. J. (2006). Exact solutions for the free in-plane vibration of rectangular plates with two opposite edges simply supported. J. Sound Vib. **294**(1): 131-161. https://doi.org/10.1016/j.jsv.2005.10.023
Gorman D. J. (2009). Accurate in-plane free vibration analysis of rectangular orthotropic plates. J. Sound Vib. **323**(1): 426-443. https://doi.org/10.1016/j.jsv.2008.12.021
Hu Z., Du J., Liu M., Li Y., Wang Z., Zheng X., Quoc Bui T., Li R. (2023). Symplectic superposition solutions for free in-plane vibration of orthotropic rectangular plates with general boundary conditions. Sci. Rep. **13**(1): 2601. https://doi.org/10.1038/s41598-023-29044-7
Huang C. S., Lee M. C., Chang M. J. (2018). Vibration and Buckling Analysis of Internally Cracked Square Plates by the MLS-Ritz Approach. Int. J. Struct. Stab. Dyn. **18**(09): 1850105. https://doi.org/10.1142/S0219455418501055
Huang C. S., Leissa A. W. (2009). Vibration analysis of rectangular plates with side cracks via the Ritz method. J. Sound Vib. **323**(3): 974-988. https://doi.org/10.1016/j.jsv.2009.01.018
Huang C. S., Leissa A. W., Chan C. W. (2011). Vibrations of rectangular plates with internal cracks or slits. Int. J. Mech. Sci. **53**(6): 436-445. https://doi.org/10.1016/j.ijmecsci.2011.03.006
Huang C. S., Lin Y. (2016). Fourier series solutions for vibrations of a rectangular plate with a straight through crack. Appl. Math. Modell. **40**(23-24): 10389-10403. https://doi.org/10.1016/j.apm.2016.07.004

Khadem S. E., Rezaee M. (2000). Introduction of modified comparison functions for vibration analysis of a rectangular cracked plate. J. Sound Vib. **236**(2): 245-258. https://doi.org/10.1006/jsvi.2000.2986
Krawczuk M., Ostachowicz W. M. (1994). A finite plate element for dynamic analysis of a cracked plate. Comput. Methods Appl. Mech. Eng. **115**(1): 67-78. https://doi.org/10.1016/0045-7825(94)90187-2
Leung R. C. N., Pinnington R. J. (1987). Vibration of a rotating disc subjected to an in-plane force at its rim, or at its centre. J. Sound Vib. **114**(2): 281-295. https://doi.org/10.1016/S0022-460X(87)80154-2
Li W., Zhang X., Du J., Liu Z. (2009). An exact series solution for the transverse vibration of rectangular plates with general elastic boundary supports. J. Sound Vib. **321**(1-2): 254-269. https://doi.org/10.1016/j.jsv.2008.09.035
Liew K. M., Hung K. C., Lim M. K. (1994). A solution method for analysis of cracked plates under vibration. Eng. Fract. Mech. **48**(3): 393-404. https://doi.org/10.1016/0013-7944(94)90130-9
Lyon R. H. (1986). In-plane contribution to structural noise transmission. Noise Control Eng. J. **26**(1): 22-27. https://doi.org/10.3397/1.2827659
Natarajan S., Baiz P. M., Bordas S., Rabczuk T., Kerfriden P. (2011). Natural frequencies of cracked functionally graded material plates by the extended finite element method. Compos. Struct. **93**(11): 3082-3092. https://doi.org/10.1016/j.compstruct.2011.04.007
Nezu K. (1982). Free Vibration of a Simply-supported Rectangular Plate with a Straight Through-notch. Bulletin of JSME **25**(199): 16-23. https://doi.org/10.1299/jsme1958.25.16
Qian G.-L., Gu S.-N., Jiang J.-S. (1991). A finite element model of cracked plates and application to vibration problems. Computers & Structures **39**(5): 483-487. https://doi.org/10.1016/0045-7949(91)90056-R
Solecki R. (1983). Bending vibration of a simply supported rectangular plate with a crack parallel to one edge. Eng. Fract. Mech. **18**(6): 1111-1118. https://doi.org/10.1016/0013-7944(83)90004-8
Song Y., Xue K., Li Q. (2022). A solution method for free vibration of intact and cracked polygonal thin plates using the Ritz method and Jacobi polynomials. J. Sound Vib. **519**: 116578. https://doi.org/10.1016/j.jsv.2021.116578
Stahl B., Keer L. (1972). Vibration and stability of cracked rectangular plates. Int. J. Solids Struct. **8**(1): 69-91. https://doi.org/10.1016/0020-7683(72)90052-2
Sun X., Ilanko S., Mochida Y., Tighe R. C. (2024). A study on the feasibility of natural frequency-based crack detection. Applied Sciences **14**(24). https://doi.org/10.3390/app142411712
Wang G., Wereley N. M. (2002). Free in-plane vibration of rectangular plates. AIAA Journal **40**(5): 953-959. https://doi.org/10.2514/2.1732
Xing Y. F., Liu B. (2009). Exact solutions for the free in-plane vibrations of rectangular plates. Int. J. Mech. Sci. **51**(3): 246-255. https://doi.org/10.1016/j.ijmecsci.2008.12.009
Yuan J., Dickinson S. (1992). The flexural vibration of rectangular plate systems approached by using artificial springs in the Rayleigh-Ritz method. J. Sound Vib. **159**(1): 39-55. https://doi.org/10.1016/0022-460X(92)90450-C
Zhong R., Wang Q., Huang Z., Chen L., Shao W., Shuai C. (2023). In-Plane Dynamic Analysis of Complex-Shaped Laminated Cracked Plates with Irregular Holes. AIAA Journal **61**(7): 3172-3189. https://doi.org/10.2514/1.J062774